Nonperturbative vibrational energy relaxation effects on vibrational line shapes

Shilong Yang, Jiushu Shao,[a] Jianshu Cao[b]
Department of Chemistry, Massachusetts Institute of Technology, Cambridge, Massachusetts 02139

(Received 7 June 2004; accepted 10 September 2004)

A general formulation of nonperturbative quantum dynamics of solutes in a condensed phase is proposed to calculate linear and nonlinear vibrational line shapes. In the weak solute-solvent interaction limit, the temporal absorption profile can be approximately factorized into the population relaxation profile from the off-diagonal coupling and the pure-dephasing profile from the diagonal coupling. The strength of dissipation and the anharmonicity-induced dephasing rate are derived in Appendix A. The vibrational energy relaxation (VER) rate is negligible for slow solvent fluctuations, yet it does not justify the Markovian treatment of off-diagonal contributions to vibrational line shapes. Non-Markovian VER effects are manifested as asymmetric envelops in the temporal absorption profile, or equivalently as side bands in the frequency domain absorption spectrum. The side bands are solvent-induced multiple-photon effects which are absent in the Markovian VER treatment. Exact path integral calculations yield non-Lorentzian central peaks in absorption spectrum resulting from couplings between population relaxations of different vibrational states. These predictions cannot be reproduced by the perturbative or the Markovian approximations. For anharmonic potentials, the absorption spectrum shows asymmetric central peaks and the asymmetry increases with anharmonicity. At large anharmonicities, all the approximation schemes break down and a full nonperturbative path integral calculation that explicitly accounts for the exact VER effects is needed. A numerical analysis of the O–H stretch of HOD in D_2O solvent reveals that the non-Markovian VER effects generate a small recurrence of the echo peak shift around 200 fs, which cannot be reproduced with a Markovian VER rate. In general, the nonperturbative and non-Markovian VER contributions have a stronger effect on nonlinear vibrational line shapes than on linear absorption. © *2004 American Institute of Physics.*
[DOI: 10.1063/1.1812748]

I. INTRODUCTION

Vibrational phase and energy relaxation of molecules in solution plays an essential role in chemical and biological processes. The energy transfer in and out of vibrational modes is closely related to reaction dynamics in condensed phases. To probe the solute-solvent interactions, extensive experimental studies have been carried out using time resolved laser spectroscopy, in particular, ultrafast laser spectroscopy.[1–12] Here we consider a simple model of vibrational relaxation of a dilute diatomic solute in a solvent. For this system, the Hamiltonian can be separated into solute, solvent, and solute-solvent interaction contributions. The standard approach to vibrational phase and energy relaxation is based on perturbation theory and Fermi's golden rule.[13] In this approach, the vibrational energy relaxation (VER) rate constant between a pair of system eigenstates is proportional to the Fourier transform of the quantum force-force correlation function calculated at the corresponding energy gap. In reality, the classical force correlation function from conventional molecular dynamics simulations is often used.[14–23] This approach does not yield quantitative agreement with experimental results although semiempirical quantum correction factors can significantly improve the agreement.[16,18,24] Another standard approach uses a classical description of the solute oscillator and a generalized Langevin equation to describe the coupling of the vibration to the bath.[25,26] This approach is valid at high temperatures or at low frequencies. In the limit of strong solute-solvent interactions, the contribution of the higher-order perturbations is crucial and these approaches break down.

Optical line shapes in condensed phases have been the subject of extensive experimental and theoretical studies. Kubo, Anderson and many others introduced the stochastic line shape theory to study two-level electronic transitions.[27–29] Modern femtosecond laser techniques can probe the intermolecular and intramolecular vibrations directly. Spectral line shapes from nonlinear spectroscopy, such as hole burning, photon-echo, pump-probe, provide important information of dynamical processes in condensed phases. Mukamel and co-workers introduced the Brownian oscillator model to describe the coupling between a two-level system and a stochastic bath. The theoretical formulation they developed have been applied to interpret a wide range of spectroscopic experiments.[4,12,30–34] Recently, Cho, Sung, and Silbey have extended the Brownian oscillator model to a multilevel system coupled to a bath with arbitrary time scales.[35,36] Con-

[a]Permanent address: State Key Laboratory of Molecular Reaction Dynamics, Center for Molecular Science Institute of Chemistry, Chinese Academy of Science, Beijing 100080, China.
[b]Author to whom correspondence should be addressed. Electronic mail: jianshu@mit.edu

tinuous efforts by Hynes, Skinner, Stratt, and many others have been devoted to calculate the line shape function using liquid theory and simulations.[15–22] Yet, these theoretical models consider pure dephasing without a full account of VER contributions. Some recent studies include VER effects in the Markovian limit.

It is crucial to establish a reliable method that can accurately calculate vibrational line shapes and precisely predict the VER effects without the Gaussian Markovian assumptions underlying the master equation approach.[37,38] To address solute-solvent interactions and maintain a quantum description, the vibrational degree of freedom has to be treated exactly. In this paper, we propose a nonperturbative approach based on Feynman's path integral,[39] and systematically investigate the VER effects in vibrational line shapes. In the nonperturbative approach, the wave functions are propagated through the solute eigenstate space under the influence of the solvent. The wave function is then projected to the specified state using the dipole operator, and computed signals of spectroscopic measurements are averaged over all possible trajectories of bath fluctuations. For the dissipative harmonic oscillator, the nonperturbative approach gives analytical expressions and quantifies the errors introduced by different approximation schemes of VER. For the dissipative Morse potential, the nonperturbative approach demonstrates the VER effects as a function of anharmonicity. The strength of dissipation and the anharmonicity-induced dephasing rate are derived in Appendix A. In the present analysis, we only consider the fundamental transition between the ground and the first excited states. A different paper will discuss spectra of overtones and combinations in *ABA* molecules.[40]

The nonperturbative formulation of quantum dynamics we propose makes a few predictions relevant to experiments; which are as follows:

(1) The non-Markovian effects of VER generate asymmetric envelops in the temporal absorption profile, which are also manifested as side bands in the absorption spectrum.

(2) Nonperturbative calculations yield non-Lorentzian peaks in absorption spectrum. The peaks are rationalized in terms of the couplings of population relaxations from different vibrational states and provide an alternative explanation of non-Lorentzian line shapes.[41]

(3) Nonperturbative VER effects lead to non-Lorentzian broadening along the diagonal direction in the frequency domain photon-echo spectra. This phenomenon is different from the pure-dephasing-induced line broadening discussed in the literature.

(4) Quantum baths generate more coherence in the long-time profile but have less effects on the short-time profile.

(5) For anharmonic oscillators, the absorption spectrum has asymmetric central peaks, and the asymmetry increases with anharmonicity.

(6) For O–H stretch in D_2O environments, non-Markovian VER effects generate a small recurrence in the three-pulse photon-echo peak shift (3PEPS).

The rest of the paper is organized as follows: In Sec. II, we discuss the nonperturbative and perturbative calculations of vibrational line shapes, including vibrational absorption, population relaxation, and photon echo. Using a perturbative expansion, the solute-solvent interaction is decomposed into the diagonal and off-diagonal components in the solute eigen-state space, which are responsible for phase relaxation and population relaxation, respectively. In the limit of weak solute-solvent interaction, the temporal absorption profile can be approximately factorized into the population relaxation profile in pump-probe experiments and the pure-dephasing profile. The well-known relation for the dephasing rate, the population relaxation rate and the pure-dephasing rate is recovered under the Markovian approximation. In Sec. III, we apply both the perturbative and nonperturbative methods to a harmonic oscillator linearly coupled to a Gaussian bath in the absence of pure dephasing. The errors introduced by different approximation schemes are examined both analytically and numerically. Non-Markovian VER effects generate asymmetric envelops in the time-domain absorption signal which are manifested as side bands in the frequency domain spectrum. These side bands are solvent-induced multiple-photon transitions and only present in the non-Markovian treatment. The nonperturbative VER effects result in non-Lorentzian central peaks. In Sec. IV, we numerically investigate the anharmonic effects in a dissipative Morse oscillator spectra, which display asymmetric line shapes. The perturbation schemes neglect the cross terms of population relaxation and pure dephasing, and therefore deviate significantly from the exact results at large anharmonicities. In Sec. V, we examine the VER effects on 3PEPS experiments in a hydrogen-bonded system. The nonlinear 3PEPS measurement is a sensitive probe of the non-Markovian VER effects. Numerical calculations reveal a small recurrence at 200 fs, which cannot be reproduced by the Markovian VER rate. Section VI concludes our analysis.

II. GENERAL FORMALISM

For chemical reactions occurring in solutions, solvent molecules play an essential role in the dynamics of the solute. In the present paper, we consider a solute molecule with one vibrational degree of freedom embedded in an environment of solvent atoms or molecules. The complete Hamiltonian is

$$H = H_s + H_b + V_{sb}, \tag{2.1}$$

where the vibrational mode is referred to as the system H_s, all the remaining degrees of freedom are considered as the bath H_b, and the coupling between them is the solute-solvent interaction V_{sb}. The system Hamiltonian is diagonalized by a set of eigenstates $|n\rangle$ with eigenenergies E_n. In the interaction picture, the solute-solvent interaction becomes a time-dependent operator $V(t) = e^{i(H_s+H_b)t} V_{sb} e^{-i(H_s+H_b)t}$. The central quantity in calculating vibrational spectra is the propagator given in the interaction picture

$$\begin{aligned} \langle n|G(t)|n\rangle &= \langle n|e^{-iHt}|n\rangle \\ &= e^{-iE_n t} e^{-iH_b t} \\ &\quad \times \left\langle \mathcal{T} \exp\left(-i \int_0^t V(\tau) d\tau \right) \right\rangle_n , \end{aligned} \tag{2.2}$$

where $\mathcal{T}$ is the chronological ordering operator, and $\langle\cdots\rangle_n = \langle n|\cdots|n\rangle$ stands for the expectation value of the nth vibrational state. Unless specified, $\hbar$ is unity implicitly. In the nonperturbative approach, the time-dependent solute-solvent interaction $V(\tau)$ is evaluated explicitly at every time step during the course of wave function propagation. Here $|n\rangle$ stands for the unperturbed system basis set while in real systems the basis set is mixed with system-bath couplings. This mixing of wave functions is inconsequential for the standard VER rate treatment, but has substantial effects on nonperturbative VER treatment. In gas phase, only $\Delta\nu=1$ transition is allowed for linear dipole operator if the system is initially in ground state. However, the system-bath coupling modifies the dipole interaction operator in the system basis set and induces multiple-photon transitions. As a result, the central peak in the absorption line shape is non-Lorentzian, and there are also solvent-induced side bands corresponding to $\Delta\nu=0, 2,\ldots$.

A. Formal definitions of vibrational line shapes

The propagator in Eq. (2.2) is used to derive expressions of vibrational spectroscopic measurements, in particular, absorption spectrum, pump-probe signals, and photon echo. These expressions not only are useful for present analysis, but also provide the basis for more reliable numerical simulations. We will demonstrate the latter aspect in future publications. Here we assume that each application of the laser field results in one vibrational transition, so that the excitation pathway can be established unambiguously.

1. Absorption spectrum

Among vibrational spectroscopic measurements, absorption is one of the most important probes of relaxation. The time-domain absorption amplitude is defined as

$$A_{\mathrm{abs}}(t)=\sum_n \langle\langle n+1|G(t)|n+1\rangle\rho_n\langle n|G(t)|n\rangle^\dagger\rangle_b$$

$$=\sum_n \rho_n A_{n,n+1,\mathrm{abs}}(t), \tag{2.3}$$

where $\langle\cdots\rangle_b$ represents the thermal average over the bath degrees of freedom and Σ_n is the sum over the solute vibrational degree of freedom. Initially the bath is in thermal equilibrium. The real part of the absorption amplitude is related to the free-induction decay signal, and the Fourier transform of absorption amplitude yields the absorption spectrum

$$A_{\mathrm{abs}}(\omega)=\mathrm{Re}\int_0^\infty A_{\mathrm{abs}}(t)e^{i\omega t}dt, \tag{2.4}$$

which can be measured by the Fourier transformed infrared (IR) spectroscopy.

2. Pump-probe signal

In a pump-probe experiment, one molecule is excited vibrationally and the subsequent vibrational relaxation transfers vibrational energy to other degrees of freedom of the original excited molecule and its neighboring molecules. Here we treat the population transfer from the nth to (n+1)th vibrational states. The pump-probe signal is given as

$$I_{\mathrm{pp}}=\sum_n \rho_n\langle|\langle n+1|G(t)|n+1\rangle|^2\rangle_b . \tag{2.5}$$

For later applications, we also write the pump-probe signal as $I_{\mathrm{pp}}(t)=\Sigma_n\rho_n I_{n+1,\mathrm{pop}}(t)$, with $I_{n,\mathrm{pop}}$ the population relaxation profile defined as

$$I_{n,\mathrm{pop}}(t)=\langle|\langle n|G(t)|n\rangle|^2\rangle_b . \tag{2.6}$$

The infrared-Raman technique developed by Laubereau and Kaiser,[1] which uses resonant vibrational pumping by a tunable mid-IR pulse and a subsequent probe by an incoherent anti-Stokes Raman, provides a powerful tool to study VER. Recently advances in ultrafast laser technology allows the IR technique to reach its full potential. Yet, it is important to note that the anti-Stokes Raman spectra also include other excitations generated by vibration-rotation couplings not included in our model.

3. Photon echo

The photon-echo measurement is a sensitive probe of homogeneous dephasing and an important example of nonlinear spectroscopy. In two-pulse photon-echo (2PE) experiments, two coherent laser pulses interact with a sample at a well-controlled time separation. The first pulse creates a coherent ensemble of atomic or molecular polarization, which dephases during the waiting time interval. The second pulse partially rephases the lost coherence and creates an echo signal. The simple version of a photon-echo experiment is a resonant third-order process with zero intermediate waiting time. The three-pulse photon-echo (3PE) measurement with a finite waiting time is discussed later in Sec. V. Let us assume that the spectral resolution is sufficiently high to resolve all the possible excitation pathways in a molecular system. For the purpose of demonstration, we consider a simple excitation pathway, $\rho_{nn}\rightarrow\rho_{n+1,n}\rightarrow\rho_{n,n+1}\rightarrow\rho_{nn}$, which is described by

$$A_{\mathrm{echo}}(t_1,t_2)=\langle\langle n|e^{-iHt_2}|n\rangle\langle n+1|e^{-iHt_1}|n+1\rangle \times\langle n|e^{-iHt_1}|n\rangle^\dagger\langle n+1|e^{-iHt_2}|n+1\rangle^\dagger\rangle_b . \tag{2.7}$$

By carrying out a series of detection experiments, one can obtain the real part, the imaginary part, or the amplitude of $A_{\mathrm{echo}}(t_1,t_2)$ in Eq. (2.7), respectively.

4. Path integral evaluation

The expressions of the vibrational spectroscopic measurements provide the basis for numerical evaluations. In these calculations, we generate time trajectories of system-bath interaction $V(t)$ and evaluate the propagator $G(t)$ along each trajectory. Then, we calculate the spectroscopic signals and average over all the trajectories. For a classical bath, one can exactly simulate the bath degree of freedom using conventional molecular dynamics techniques, generate a time-dependent force through the system-bath coupling, and propagate the quantum vibrational degree of freedom ex-

actly. Due to the intrinsic complexity of quantum baths, an exact simulation of the bath modes is not yet available.[42] But for vibrational line shapes, as shown later, a quantum representation of bath degrees of freedom is not necessary at room temperatures. Hence, we can propagate quantum vibrational degree of freedom under classical force of the bath. Another technique, the surface hopping method, is used widely to treat a classical anharmonic bath coupled to a quantum system.[43–47] In the present paper we focus on a Gaussian bath linearly coupled to the system. Linearized dissipative models have been applied extensively to study dynamic processes in condensed phases, including activated dynamics, electron and proton transfer, diffusion, and vibrational energy relaxation. For a Gaussian bath, several numerical techniques can be applied, which are as follows.

(1) For a Uhlenbeck process, the force-force correlation function is exponential, i. e., $C(t)=\langle \delta f^2\rangle_b e^{-\gamma t}$. The propagation of random force is a Markovian process satisfying $G_f(f,t|f',t')=\int_{-\infty}^{\infty} G_f(f,t|f'',t'')G_f(f'',t''|f',t')df''$, where the Green's function of random force is a Gaussian distribution

$$G_f(f,t|f',t')=[2\pi\langle \delta f^2\rangle_b(1-e^{-2\gamma(t-t')})]^{-1/2} \times\exp\left[-\frac{(f-f'e^{-\gamma(t-t')})^2}{2\langle \delta f^2\rangle_b(1-e^{-2\gamma(t-t')})}\right]. \tag{2.8}$$

The equilibrium distribution of the random force is $P_{\mathrm{eq}}(f)=[2\pi\langle \delta f^2\rangle_b]^{-1/2}\exp[-f^2/2\langle \delta f^2\rangle_b]$, assuming that the random force has a zero mean. With the Markovian property, one can generate a number of random force trajectories by first generating $f(t_0)$ from the equilibrium distribution and then using Eq. (2.8) to generate the random forces at subsequent time steps. The quantum system of vibrational degrees of freedom is propagated along each trajectory, and vibrational line shapes are calculated exactly. The bath average is obtained through an average over all the trajectories.

(2) For a set of linearly coupled harmonic oscillators, one can always identify the normal coordinates of the bath through an orthogonal transform, and each normal mode is a Uhlenbeck process. For example, we use biexponential friction kernel in the O–H relaxation. Hence, one can first generate the normal coordinates using the method in (1) and then generate the bath modes using the orthogonal transform.

(3) For a quantum Gaussian bath, integration of the bath modes leads to influence functionals which couples the system variables at different times. As a numerical technique, the influence functional formalism[48] becomes tedious when multiple excitations are involved. As an alternative, the method proposed by Cao, Ungar, and Voth[49] samples the Gaussian random force directly without introducing the influence functional formalism and propagates the system under the influence of quantum forces. This method is particularly adequate for complicated multiple-time propagation of a vibrational system.

B. Perturbative expressions: Factorization and cumulant expansion

1. Factorization

In the perturbative approach, we decompose the system-bath coupling $V(t)$ into the diagonal and the off-diagonal operators in the vibrational eigenspace, giving

$$V_D(t)=\sum_n \langle V(t)\rangle_n|n\rangle\langle n| \tag{2.9a}$$

and

$$V_{\mathrm{OD}}(t)=V(t)-V_D(t). \tag{2.9b}$$

The corresponding propagator can be written as

$$\begin{aligned}\langle n|G(t)|n\rangle &\approx e^{-iE_nt}e^{-iH_bt}\langle n|\mathcal{T}\exp\left(-i\int_0^t V_D(\tau)d\tau\right)\\ &\quad\times\mathcal{T}\exp\left(-i\int_0^t V_{\mathrm{OD}}(\tau)d\tau\right)|n\rangle\\ &=e^{-iE_nt}e^{-iH_bt}\mathcal{T}\exp\left(-i\int_0^t\langle V_D(\tau)\rangle_n d\tau\right)\\ &\quad\times\left\langle\mathcal{T}\exp\left(-i\int_0^t V_{\mathrm{OD}}(\tau)d\tau\right)\right\rangle_n .\end{aligned} \tag{2.10}$$

In Eq. (2.10), we decompose the exponential function of two time-dependent operators into the product of the two corresponding exponentials, which is valid only if $V_D(t)$ and $V_{\mathrm{OD}}(t)$ commute. The approximation neglects the contribution from $[V_D(t),V_{\mathrm{OD}}(t)]$, which is generally nonzero for anharmonic potentials. In Sec. IV we demonstrate quantitatively that $[V_D(t),V_{\mathrm{OD}}(t)]$ increases with anharmonicity and results in large deviations between the perturbative and the exact results.

We now apply the decomposition in Eq. (2.10) to the vibrational line shapes in Sec. II A and derive the perturbative expressions for the temporal absorption profile, population relaxation profile, and photon echo. The absorption amplitude in Eq. (2.3) can be rewritten as

$$\begin{aligned}A_{n,n+1,\mathrm{abs}}(t)&\approx e^{-i\Omega_{n,n+1}t}\left\langle\mathcal{T}\exp\left(-i\int_0^t\omega_{n,n+1}(\tau)d\tau\right)\right\rangle\left\langle\mathcal{T}\exp\left(-i\int_0^t V_{\mathrm{OD}}(\tau)d\tau\right)\right\rangle_{n+1}\left\langle\mathcal{T}\exp\left(-i\int_0^t V_{\mathrm{OD}}(\tau)d\tau\right)\right\rangle_n^{\dagger}\Big\rangle_b\\ &\approx e^{-i\Omega_{n,n+1}t}\left\langle\mathcal{T}\exp\left(-i\int_0^t\omega_{n,n+1}(\tau)d\tau\right)\right\rangle_b\left\langle\left\langle\mathcal{T}\exp\left(\int_0^t V_{\mathrm{OD}}(\tau)d\tau\right)\right\rangle_{n+1}\right\rangle_b\left\langle\left\langle\mathcal{T}\exp\left(\int_0^t V_{\mathrm{OD}}(\tau)d\tau\right)\right\rangle_n\right\rangle_b^{\dagger},\end{aligned} \tag{2.11}$$

where $\Omega_{n,n+1}=E_{n+1}-E_n$ is the frequency gap and $\omega_{n,n+1}(t)=\langle V_D(t)\rangle_{n+1}-\langle V_D(t)\rangle_n^*$ is the diagonal frequency difference induced by the solute-solvent interaction. In Eq. (2.11), we first decouple the bath averages of the diagonal and the off-diagonal parts, then perform the bath average on each propagator separately. As discussed in Eq. (2.10), the first approximation neglects the commutator between $V_D(t)$ and $V_{\mathrm{OD}}(t')$. The second approximation neglects the cross terms between the propagators and is correct only for weak solute-solvent interactions.

With the propagator in Eq. (2.10), the population relaxation profile in Eq. (2.6) reduces to

$$I_{n,\mathrm{pop}}(t)\approx\left\langle\left|\langle n|\mathcal{T}\exp\left(-i\int_0^t V_{\mathrm{OD}}(\tau)d\tau\right)|n\rangle\right|^2\right\rangle_b \approx\left\langle\langle n|\exp\left(-i\int_0^t V_{\mathrm{OD}}(\tau)d\tau\right)|n\rangle\right\rangle_b \times\left\langle\langle n|\exp\left(-i\int_0^t V_{\mathrm{OD}}(\tau)d\tau\right)|n\rangle^\dagger\right\rangle_b =\left|\langle n|\left\langle\exp\left(-i\int_0^t V_{\mathrm{OD}}(\tau)d\tau\right)\right\rangle_b|n\rangle\right|^2. \tag{2.12}$$

Comparing the above equation with Eq. (2.11), we realize that

$$A_{n,n+1,\mathrm{abs}}(t)\approx e^{i\Omega_{n,n+1}t}\sqrt{I_{n,\mathrm{pop}}(t)I_{n+1,\mathrm{pop}}(t)}\times A_{n,n+1,\mathrm{dep}}(t), \tag{2.13}$$

where $A_{n,n+1,\mathrm{dep}}(t)=\langle\exp[-i\int_0^t\omega_{n,n+1}(\tau)d\tau]\rangle_b$ is the contribution from pure dephasing. Equation (2.13) demonstrates that temporal absorption profile can be approximately factorized into the population relaxation profile and the pure-dephasing profile. As a result, the off-diagonal part of the interaction, $V_{\mathrm{OD}}(t)$, contributes to population relaxation, and the diagonal part of the interaction, $V_D(t)$, contributes to pure dephasing.

Inserting Eq. (2.10) into the photon-echo expression defined in Eq. (2.7) and following the same factorization scheme as Eq. (2.11), we arrive at

$$\begin{aligned}A_{\mathrm{echo}}(t_1,t_2)\approx{}& e^{i\Omega_{n,n+1}(t_2-t_1)}\left\langle\left[\exp\left[\left(i\int_{t_1}^{t_1+t_2}\omega_{n,n+1}^*(\tau)d\tau\right)-\left(i\int_0^{t_1}\omega_{n,n+1}(\tau)d\tau\right)\right]\left\langle\mathcal{T}\exp\left(-i\int_{t_1}^{t_1+t_2}V_{\mathrm{OD}}(\tau)d\tau\right)\right\rangle_n\right.\right.\\ &\left.\left.\times\left\langle\mathcal{T}\exp\left(-i\int_0^{t_1}V_{\mathrm{OD}}(\tau)d\tau\right)\right\rangle_{n+1}\left\langle\mathcal{T}\exp\left(-i\int_0^{t_1}V_{\mathrm{OD}}(\tau)d\tau\right)\right\rangle_n^\dagger\left\langle\mathcal{T}\exp\left(-i\int_{t_1}^{t_1+t_2}V_{\mathrm{OD}}(\tau)d\tau\right)\right\rangle_{n+1}^\dagger\right]\right\rangle_b\\ \approx{}& e^{i\Omega_{n,n+1}(t_2-t_1)}\left\langle\exp\left[\left(i\int_{t_1}^{t_1+t_2}\omega_{n,n+1}(\tau)d\tau\right)-\left(\int_0^{t_1}\omega_{n,n+1}(\tau)d\tau\right)\right]\right\rangle_b\left\langle\left\langle\mathcal{T}\exp\left(-i\int_{t_1}^{t_1+t_2}V_{\mathrm{OD}}(\tau)d\tau\right)\right\rangle_n\right\rangle_b\\ &\times\left\langle\left\langle\mathcal{T}\exp\left(-i\int_0^{t_1}V_{\mathrm{OD}}(\tau)d\tau\right)\right\rangle_{n+1}\right\rangle_b\left\langle\left\langle\mathcal{T}\exp\left(-i\int_0^{t_1}V_{\mathrm{OD}}(\tau)d\tau\right)\right\rangle_n\right\rangle_b^\dagger\\ &\times\left\langle\left\langle\mathcal{T}\exp\left(-i\int_{t_1}^{t_1+t_2}V_{\mathrm{OD}}(\tau)d\tau\right)\right\rangle_{n+1}\right\rangle_b^\dagger,\end{aligned} \tag{2.14}$$

where the photon-echo signal is also decomposed into the population relaxation contribution from the off-diagonal interaction and the pure-dephasing contribution from the diagonal interaction.

2. Second-order cumulant expansion

To further simplify the analysis, we truncate the solute-solvent interaction to second order of bath fluctuation, which is valid for weak solute-solvent interactions or fast bath relaxations. First, the temporal profile for population relaxation from the nth vibrational state is approximated by taking the bath average $\langle\cdots\rangle_b$ for each propagator in Eq. (2.12) separately, giving

$$I_{n,\mathrm{pop}}(t)\approx\left|\langle n|\left\langle\exp\left(-i\int_0^t V_{\mathrm{OD}}(\tau)d\tau\right)\right\rangle_b|n\rangle\right|^2 \approx|\exp[-h_n(t)]|^2, \tag{2.15}$$

where $h_n(t)=\int_0^t\int_0^\tau\langle n|\langle V_{\mathrm{OD}}(t_1)V_{\mathrm{OD}}(t_2)\rangle_b|n\rangle dt_1\,dt_2$ characterizes the population relaxation from the nth vibrational state. The last approximation switches the exponential function and quantum expectation value after invoking the cumulant expansion, and assumes a diagonal form of $\langle V_{\mathrm{OD}}(t_1)V_{\mathrm{OD}}(t_2)\rangle_b$ while neglecting its off-diagonal elements.

Similarly, application of the second-order cumulant expansion to the pure-dephasing profile leads to

$$A_{n,n+1,\mathrm{dep}}(t)=\left\langle \exp\left[-i\int_0^t \omega_{n,n+1}(\tau)d\tau\right]\right\rangle_b \approx \exp[-i\langle\omega_{n,n+1}\rangle_b t-g(t)], \tag{2.16}$$

where $g(t)=\int_0^t\int_0^\tau\langle\delta\omega_{n,n+1}(t_1)\delta\omega_{n,n+1}(t_2)\rangle_b dt_1\,dt_2$ is the line shape function and $\langle\omega_{n,n+1}\rangle_b$ is the Stokes shift. Combining the population relaxation profile and the pure-dephasing signal, the absorption amplitude in Eq. (2.11) reduces to

$$A_{n,n+1,\mathrm{abs}}(t)\approx e^{-i\Omega_{n,n+1}t}\exp[-i\langle\omega_{n,n+1}\rangle_b t-g(t)-h_n^*(t)-h_{n+1}(t)]. \tag{2.17}$$

The 2PE signal in Eq. (2.14) after the second-order cumulant expansion becomes

$$\begin{aligned}A_{\mathrm{echo}}(t_1,t_2)\approx{}& e^{i\Omega_{n,n+1}(t_2-t_1)}\exp[i\langle\omega_{n,n+1}\rangle_b(t_2-t_1)\\ &-2g^*(t_1)-g(t_2)-g^*(t_2)+g^*(t_1+t_2)]\\ &\times\exp[-h_{n+1}(t_1)-h_n(t_2)-h_n^*(t_1)\\ &-h_{n+1}^*(t_2)].\end{aligned} \tag{2.18}$$

In the limit $h_n(t)\to 0$, Eq. (2.18) reduces to the well-known 2PE expression for a two-level system.[4] A generalization of Eq. (2.18) to an arbitrary number of vibrational states in the limit of $h_n(t)\to 0$ was recently proposed by Sung and Silbey.[36] Their treatment includes diagonal matrix elements only while VER effects are absent.

In many cases, composite approximation schemes are adopted to explain the vibrational measurements. The decomposition relation in Eq. (2.13) and the second-order cumulant expansion yield

$$A_{n,n+1,\mathrm{abs}}(t)\approx[I_{n,\mathrm{pop}}(t)I_{n+1,\mathrm{pop}}(t)]^{1/2}\times\exp[-i\Omega_{n,n+1}t-i\langle\omega_{n,n+1}\rangle_b t-g(t)]. \tag{2.19}$$

The advantage of this decomposition is that the population relaxation profile is measured from pump-probe experiments and contains nonperturbative information of VER. As we will demonstrate later that the decomposition yields results close to nonperturbative calculations, accurately reproducing the short-time oscillations. But this approximation neglects the cross terms between the population relaxations from the nth and the $(n+1)$th states and the coupling between population relaxation and pure dephasing, and does not contain any phase information of VER. Because of these approximations, Eq. (2.19) cannot reproduce asymmetric absorption spectra for anharmonic systems.

C. Markovian approximation

The essence of Markovian approximation is that the relaxation of the vibrational degree of freedom is much slower than the relaxation of bath modes. Under the Markovian limit, the line shape function and the population relaxation exponent are linearly increasing with time, i.e.,

$$g(t)\approx\Gamma'_{n,n+1}t, \tag{2.20a}$$

and

$$h_n(t)\approx\frac{\Gamma_n}{2}t, \tag{2.20b}$$

where $\Gamma'_{n,n+1}=\int_0^\infty\langle\delta\omega_{n,n+1}(t)\delta\omega_{n,n+1}(0)\rangle_b dt$ and $\Gamma_n=2\int_0^\infty\langle n|\langle V_{\mathrm{OD}}(\tau)V_{\mathrm{OD}}(0)\rangle_b|n\rangle d\tau$ are usually complex, with the real part being the population relaxation rate and the imaginary part being the frequency shift. Consequently, the population relaxation profile is approximated by an exponential function $I_{n,\mathrm{pop}}(t)\approx\exp[-\mathrm{Re}(\Gamma_n)t]$, and the pure-dephasing profile becomes $A_{n,n+1,\mathrm{dep}}(t)\approx\exp[-\Gamma'_{n,n+1}t-i\langle\omega_{n,n+1}\rangle_b t]$. In Eq. (2.17), the absorption profile is approximated by $A_{n,n+1,\mathrm{abs}}(t)\approx\exp[-i\Omega_{n,n+1}-i\langle\omega_{n,n+1}\rangle_b t-\Gamma_{n,n+1}t]$ with $\Gamma_{n,n+1}=(\Gamma_n^*+\Gamma_{n+1})/2+\Gamma'_{n,n+1}$. Thus, the time-dependent expression of Eq. (2.13) recovers the well-known relation

$$k_{n,n+1}=\frac{k_n+k_{n+1}}{2}+k'_{n,n+1}, \tag{2.21}$$

where $k_n=\mathrm{Re}(\Gamma_n)$ is the population relaxation rate, $k'_{n,n+1}=\mathrm{Re}(\Gamma'_{n,n+1})$ is the pure-dephasing rate, and $k_{n,n+1}=\mathrm{Re}(\Gamma_{n,n+1})$ is the dephasing rate. Under the Markovian approximation, the photon-echo signal is readily simplified as

$$\begin{aligned}A_{\mathrm{echo}}(t_1,t_2)\approx{}& e^{i\Omega_{n,n+1}(t_2-t_1)}\exp[-i\langle\omega_{n,n+1}\rangle_b(t_2-t_1)\\ &-\Gamma'_{n,n+1}t_2-\Gamma'^*_{n,n+1}t_1]\\ &\times\exp\left[-\frac{\Gamma_{n+1}+\Gamma_n^*}{2}t_1-\frac{\Gamma_n+\Gamma_{n+1}^*}{2}t_2\right].\end{aligned} \tag{2.22}$$

Considering that pure dephasing in anharmonic potentials is much faster than population relaxation, we can approximate the population relaxation with the Markovian rate and the pure-dephasing signal with second-order cumulant expansion

$$A_{n,n+1,\mathrm{abs}}(t)\approx e^{-i\Omega_{n,n+1}t}\exp\left[-i\langle\omega_{n,n+1}\rangle_b t-g(t)-\frac{\Gamma_n^*}{2}t-\frac{\Gamma_{n+1}}{2}t\right]. \tag{2.23}$$

For the dissipative harmonic oscillator discussed later in Sec. IV, the diagonal couplings are 0 and $A_{n,n+1,\mathrm{dep}}(t)=1$, and equation (2.23) becomes identical to the Markovian approximation. For a dissipative Morse potential in Sec. V, the deviations of Eqs. (2.19) and (2.23) from the nonperturbative results increase with anharmonicity.

D. Inconsistency of the Markovian rate approximation of VER

Let us now discuss the physical meaning of $h_n(t)$. Usually the solvent relaxation rate γ, the VER rate, pure-dephasing rate, and the vibrational frequency satisfy $\Omega_{n,n+1}>k'_{n,n+1}>k_n>\gamma$. The population relaxation process occurs through the resonance between the vibrational frequency and the bath spectrum while the dephasing rate corresponds to the bath spectrum at zero frequency. Given the fact that $\gamma\ll\Omega_{n,n+1}$, vibrational relaxation is much slower than pure dephasing, hence $k'_{n,n+1}\gg k_n$ and the line shapes

are usually dominated by pure dephasing. In this case, vibrational relaxation is either ignored or approximated with a Markovian rate. However, this argument is not self-consistent because the Markovian rate approximation is only valid at sufficient long time while the vibrational line shape generally depends on the full time history of the off-diagonal contribution.

To illustrate this point, we consider a linear system-bath coupling $f(t)q$, which will be further investigated in later sections. The second-order cumulant expansion gives

$$h_n(t)=\sum_{m\neq n}\frac{\langle\delta f^2\rangle_b q_{nm}^2}{\hbar^2}\int_0^t(t-\tau)e^{-\gamma t}\cos\,\Omega_{mn}\tau d\tau. \quad (2.24)$$

In the limit of a fast bath, $h_n(t)\approx\gamma t(\Sigma_{m\neq n}\langle\delta f^2\rangle_b q_{nm}^2/\hbar^2\Omega_{mn}^2)$ and yields a Markovian rate. In the limit of a frozen bath $\gamma\to 0$, $h_n(t)\approx\Sigma_{m\neq n}\langle\delta f^2\rangle_b q_{nm}^2(1-\cos\,\Omega_{mn}t)/\hbar^2\Omega_{mn}^2$, which leads to side bands with $\Delta\omega=\Omega_{mn}$ around the central peak in the vibrational line shapes. As we mentioned in Sec. II, the side bands are induced by the system-bath coupling. Apparently $h_n(t)$ is intrinsically oscillatory over the complete time domain while the Markovian approximation implies $h_n(t)\to 0$ and $k_n\to 0$, which is obviously inadequate to describe the VER contribution. The slow bath assumption renders the Markovian description of the VER effects inadequate.

III. ANALYTICAL SOLUTIONS OF DISSIPATIVE HARMONIC OSCILLATOR

For the purpose of illustration, we first model the vibrational degree of freedom as a harmonic oscillator linearly coupled to a classical bath. The classical bath assumption is often adopted because one can always separate the degrees of freedom into those with low frequencies $\hbar\omega\leqslant k_BT$, which may be treated classically as the bath, and those with high frequencies $\hbar\omega>k_BT$, which must be treated quantum mechanically as the system. The Hamiltonian is thus given by

$$H=\frac{p^2}{2\mu}+\frac{1}{2}\omega_0^2q^2+f(t)q, \quad (3.1)$$

where $f(t)$ is a Gaussian random force resulting from the bath degree of freedom. The bath relaxation is described by the friction kernel $C_{\rm cl}(t)=\langle\delta f(t)\,\delta f(0)\rangle_b$, where the subscript represents a classical bath. Quantum effects of the Gaussian bath are discussed in Sec. III E. In numerical calculations, we assume an exponentially decaying friction kernel, $C_{\rm cl}(t)=\langle\delta f^2\rangle_b\exp[-\gamma t]$. $\langle\delta f^2\rangle_b$ is the mean square fluctuation of the random force and is a probe of the average strength of the solute-solvent interaction. The linear solute-solvent coupling here has no diagonal contribution; thus, there is no pure-dephasing contribution and all the vibrational line shapes are generated by VER. The analytical solutions offer us a good benchmark of the accuracies of various approximations.

A. Exact path integral calculation

Now we discuss the exact calculations of the vibrational line shapes defined in Sec. II. The propagator of the forced harmonic oscillator is[39]

$$\begin{aligned}G(q_2,t;q_1,0)=&\sqrt{\frac{\mu\omega_0}{2\pi i\hbar\,\sin\,\omega_0t}}\exp\left\{\frac{i\mu\omega_0}{2\hbar\,\sin\,\omega_0t}[(q_2^2+q_1^2)\cos\,\omega_0t-2q_1q_2]\right\}\\&\times\exp\left\{-\frac{i\mu\omega_0}{2\hbar\,\sin\,\omega_0t}\left[\frac{2q_1}{\mu\omega_0}\int_0^t f(\tau)\sin\,\omega_0(t-\tau)d\tau+\frac{2q_2}{\mu\omega_0}\int_0^t f(\tau)\sin\,\omega_0\tau d\tau\right]\right\}\\&\times\exp\left\{-\frac{i\mu\omega_0}{2\hbar\,\sin\,\omega_0t}\left[\frac{2}{\mu^2\omega_0^2}\int_0^t\int_0^t f(\tau)f(\tau')\sin\,\omega_0(t-\tau)\sin\,\omega_0\tau'\,d\tau\,d\tau'\right]\right\}. \quad (3.2)\end{aligned}$$

The transition moments between a pair of vibrational eigenstates are given by

$$\begin{aligned}G_{mn}(t)=&e^{i/\hbar\,E_mt}\int_{-\infty}^{\infty}\int_{-\infty}^{\infty}\phi_m(q_2)G(q_2,t;q_1,0)\\&\times\phi_n(q_1)dq_1\,dq_2\\=&\frac{G_{00}(t)}{\sqrt{m!n!}}\sum_{r=0}^{l}\frac{(-1)^{m+n}m!n!}{(m-r)!(n-r)!}(i\zeta)^{n-r}(i\zeta')^{m-r},\\&\text{with}\ \ l=\max\{m,n\},\end{aligned}$$

$$\zeta(t)=\frac{1}{\sqrt{2\mu\omega_0\hbar}}\int_0^t f(\tau)\exp[-i\omega_0\tau]d\tau, \quad (3.3a)$$

and

$$\zeta'(t)=\frac{1}{\sqrt{2\mu\omega_0\hbar}}\int_0^t f(\tau)\exp[i\omega_0\tau]d\tau. \quad (3.3b)$$

In Eqs. (3.3), $\phi_n(q)$ is the nth eigenfunction and ζ,ζ' are incomplete Fourier transforms of the random force at the fundamental frequency. The diagonal transition moment $G_{00}(t)$ for the ground state is given by $G_{00}(t)=\exp[-\zeta(t)\zeta'(t)]$. For the rest of this paper, we only consider the fundamental transition between the ground state $|g\rangle=|0\rangle$ and the first excited state $|e\rangle=|1\rangle$ unless specified otherwise. A different paper will discuss spectra of overtones and combinations in ABA molecules.[40] The absorption am-

plitude for $|g\rangle\rightarrow|e\rangle$ is thus $A_{ge,\mathrm{abs}}(t)=\langle\langle e|e^{-iHt}|e\rangle\times\langle g|e^{-iHt}|g\rangle^{\dagger}\rangle_b$. We apply Eq. (3.3) twice for $m=n=0$ and $m=n=1$, respectively, and obtain the absorption amplitude $A_{ge,\mathrm{abs}}(t)=e^{-i\omega_0 t}(1+\partial_z)|_{z=1}\langle\exp[-z\zeta(t)\zeta'(t)]\rangle_b$. For a Gaussian bath, the average can be directly calculated with the cumulant expansion, giving

$$A_{ge,\mathrm{abs}}(t)=e^{-i\omega_0 t}[1+2(\alpha_{11}+\alpha_{22})+4(\alpha_{11}\alpha_{22}-\alpha_{12}^2)]^{-3/2}(1+\alpha_{11}+\alpha_{22}),$$

where

$$\alpha_{ij}(t)=\frac{1}{\mu\omega_0\hbar}\int_0^t\int_0^\tau\langle f(\tau)f(\tau')\rangle_b\psi_i(\tau)\psi_j(\tau')d\tau\,d\tau',\quad i,j\in\{1,2\}. \tag{3.4}$$

Here, $\psi_1(\tau)$ and $\psi_2(\tau)$ are short-hand notations for $\cos\omega_0\tau$ and $\sin\omega_0\tau$, respectively. Given the exponential friction kernel, $\alpha_{ij}(t)$ can be evaluated explicitly. We find that the envelop of $A_{ge,\mathrm{abs}}(t)$ exhibits a power-law decay in the long-time limit, i. e., $A_{ge,\mathrm{abs}}(t)\approx e^{-i\omega_0 t}(1+\Gamma_{ge}t/2)^{-2}$, with Γ_{ge} equal to the dephasing rate defined later in the Markovian limit (see Sec. III C).

We use the transition amplitudes in Eq. (3.3) to evaluate the population relaxation signal in pump-probe experiments $I_{n,\mathrm{pop}}(t)$ analytically. For instance, the population relaxation profiles for the ground and the first excited states are

$$I_{g,\mathrm{pop}}(t)=[1+2(\alpha_{11}+\alpha_{22})+4(\alpha_{11}\alpha_{22}-\alpha_{12}^2)]^{-1/2}$$

and

$$I_{e,\mathrm{pop}}(t)=[1+2(\alpha_{11}+\alpha_{22})+4(\alpha_{11}\alpha_{22}-\alpha_{12}^2)]^{-5/2}\times[1+2(\alpha_{11}+\alpha_{22})+3(\alpha_{11}+\alpha_{22})^2-4(\alpha_{11}\alpha_{22}-\alpha_{12}^2)+8(\alpha_{11}+\alpha_{22})(\alpha_{11}\alpha_{22}-\alpha_{12}^2)+16(\alpha_{11}\alpha_{22}-\alpha_{12}^2)^2]. \tag{3.5}$$

In the long-time limit, it is straightforward to show that both $I_{g,\mathrm{pop}}$ and $I_{e,\mathrm{pop}}$ decays as t^{-1}.

In the absence of pure dephasing, the decomposition relation Eq. (2.13) becomes $|A_{n,n+1,\mathrm{abs}}(t)|^2\approx I_{n,\mathrm{pop}}(t)I_{n+1,\mathrm{pop}}(t)$, which is obtained under the weak coupling assumption. To explicitly check its validity, we compare the decomposition relation with the exact results from the path integral calculations. To be specific, we expand Eqs. (3.4) and (3.5) in orders of $\langle\delta f^2\rangle_b$,

$$\begin{aligned}|A_{ge,\mathrm{abs}}(t)|^2&\approx 1-4(\alpha_{11}+\alpha_{22})+13(\alpha_{11}+\alpha_{22})^2-12(\alpha_{11}\alpha_{22}-\alpha_{12}^2)+O(\langle\delta f^6\rangle_b),\\ I_{g,\mathrm{pop}}(t)I_{e,\mathrm{pop}}(t)&\approx 1-4(\alpha_{11}+\alpha_{22})+15(\alpha_{11}+\alpha_{22})^2-16(\alpha_{11}\alpha_{22}-\alpha_{12}^2)+O(\langle\delta f^6\rangle_b).\end{aligned} \tag{3.6}$$

These two quantities are equal only up to first order in $\langle\delta f^2\rangle_b$. For a harmonic oscillator linearly coupled to a classical bath, the diagonal coupling $V_D(t)$ is zero; hence, the only approximation introduced in Eq. (2.11) is the independent bath average for each propagator. The difference $2(\alpha_{11}^2+\alpha_{22}^2+2\alpha_{12}^2)$ between the two expressions in Eq. (3.6) is a quantitative measure of this assumption. The positive definite difference indicates that the decomposition relation overestimates the absorption profile in the second order of $\langle\delta f^2\rangle_b$.

The transition moments in Eq. (3.3) allow us to calculate the exact (2PE) signal in Eq. (2.7) as

$$A_{\mathrm{echo}}(t_1,t_2)=e^{i\omega_0(t_2-t_1)}(1+\partial_{z_1})|_{z_1=1}\times(1+\partial_{z_2})|_{z_2=1}[\det M(z_1,z_2)]^{-1/2}, \tag{3.7}$$

where the matrix $M(z_1,z_2)$ is

$$M(z_1,z_2)=\begin{bmatrix}1+2z_1\alpha_{11}(t_1,t_1) & 2z_1\alpha_{12}(t_1,t_1) & 2\sqrt{z_1z_2}\alpha_{11}(t_1,t_2) & 2\sqrt{z_1z_2}\alpha_{12}(t_1,t_2)\\ 2z_1\alpha_{12}(t_1,t_1) & 1+2z_1\alpha_{22}(t_1,t_1) & 2\sqrt{z_1z_2}\alpha_{12}(t_2,t_1) & 2\sqrt{z_1z_2}\alpha_{22}(t_1,t_2)\\ 2\sqrt{z_1z_2}\alpha_{11}(t_1,t_2) & 2\sqrt{z_1z_2}\alpha_{12}(t_2,t_1) & 1+2z_2\alpha_{11}(t_2,t_2) & 2z_2\alpha_{12}(t_2,t_2)\\ 2\sqrt{z_1z_2}\alpha_{12}(t_1,t_2) & 2\sqrt{z_1z_2}\alpha_{22}(t_1,t_2) & 2z_2\alpha_{12}(t_2,t_2) & 1+2z_2\alpha_{22}(t_2,t_2)\end{bmatrix}, \tag{3.8}$$

with $\alpha_{ij}(t_1,t_2)=[2\mu\omega_0\hbar]^{-1}\int_0^{t_1}\int_0^{t_2}\langle f(\tau)f(\tau')\rangle_b\times\psi_i(\tau)\psi_j(\tau')d\tau\,d\tau'$ defined similarly as in Eq. (3.4).

B. Perturbation

We now investigate the perturbation method. The diagonal matrix element of the propagator is given by

$$\langle n|e^{-iHt}|n\rangle=e^{-i\omega_n t}\langle n|\mathcal{T}\exp\left[-i\int_0^t f(\tau)q(\tau)d\tau\right]|n\rangle, \tag{3.9}$$

where $q(t)$ is the time-dependent position operator in the interaction picture. We note that, because of $V_D(t)=0$, the factorization in Eq. (2.10) becomes exact. We first neglect the cross terms between propagators and perform the bath average over each propagator separately, giving

$$A_{n,n+1,\mathrm{abs}}(t) \approx e^{-i\omega_0 t}\left\langle \langle n+1|\mathcal{T}\exp\left(-i\int_0^t f(\tau)q(\tau)d\tau\right)|n+1\rangle\right\rangle_b \times\left\langle \langle n|\mathcal{T}\exp\left(-i\int_0^t f(\tau)q(\tau)d\tau\right)|n\rangle\right\rangle_b^{\dagger}. \quad (3.10)$$

Next, we exchange the order of the bath average and the expectation value over vibrational states, and perform the second-order cumulant expansion for the Gaussian bath

$$A_{n,n+1,\mathrm{abs}}(t) \approx e^{-i\omega_0 t}\langle n+1| \times\exp\left[-\int_0^t\int_0^\tau q(\tau)q(\tau')\langle f(\tau)f(\tau')\rangle_b d\tau\, d\tau'\right] \times|n+1\rangle\langle n|\exp\left[-\int_0^t\int_0^\tau q(\tau)q(\tau') \times\langle f(\tau)f(\tau')\rangle_b d\tau\, d\tau'\right]|n\rangle. \quad (3.11)$$

Finally, we take the expectation value of the exponent, which is only accurate when the exponent is diagonal, giving

$$A_{n,n+1,\mathrm{abs}}(t)\approx e^{-i\omega_0 t}\exp[-h_{n+1}(t)-h_n^*(t)], \quad (3.12)$$

where $h_n(t)=(1/\hbar^2)\int_0^t\int_0^\tau\langle f(\tau)f(\tau')\rangle_b\langle n|q(\tau)q(\tau')|n\rangle$ characterizes the population relaxation process from the nth vibrational state. For a harmonic oscillator, $h_n(t)$ can be evaluated explicitly to be $\mu\hbar\omega_0 h_n(t)=2(n+1/2)\times\int_0^t d\tau\int_0^\tau d\tau'\langle f(\tau)f(\tau')\rangle_b\cos\omega_0(\tau-\tau')$. Particularly by setting $n=0$ in this expression, we obtain the second order cumulant expansion result for $A_{ge,\mathrm{abs}}(t)$ as

$$A_{ge,\mathrm{abs}}(t)\approx e^{-i\omega_0 t}\exp(-2[\alpha_{11}(t)+\alpha_{22}(t)]), \quad (3.13)$$

where $\alpha_{11}(t)$ and $\alpha_{22}(t)$ are defined in Eq. (3.4).

Compared to the exact path integral expression, the second-order cumulant expansion is accurate up to first order in the bath fluctuation $\langle\delta f^2\rangle_b$. The essential difference is the absence of the cross term α_{12} in the second-order cumulant expression result. To facilitate the comparison with the exact expression, we expand the square of Eq. (3.13) to second order, giving

$$|A_{ge,\mathrm{abs}}|^2=1-4(\alpha_{11}+\alpha_{22})+8(\alpha_{11}+\alpha_{22})^2+O(\langle\delta f^6\rangle_b). \quad (3.14)$$

The overall deviation from the exact result is $5(\alpha_{11}+\alpha_{22})^2-12(\alpha_{11}\alpha_{22}-\alpha_{12}^2)$, which is a combination of all the approximations in Eqs. (3.10), (3.11), and (3.12). It is readily shown that this difference is positive definite, indicating that the second-order cumulant expansion always underestimates the absorption profile.

Applying the approximations in Eqs. (3.10), (3.11), and (3.12) to Eq. (2.6), the population relaxation profile discussed in Sec. II A is $I_{n,\mathrm{pop}}(t)\approx|\exp[-h_n(t)]|^2$. Setting $n=0$ and $n=1$, we obtain the second-order cumulant expansion of the population relaxation at the ground and the first excited states, respectively,

$$I_{g,\mathrm{pop}}(t)\approx\exp(-[\alpha_{11}(t)+\alpha_{22}(t)]) \quad (3.15a)$$

and

$$I_{e,\mathrm{pop}}(t)\approx\exp(-3[\alpha_{11}(t)+\alpha_{22}(t)]). \quad (3.15b)$$

Combination of these two expressions leads to Eq. (3.13). These perturbative expressions, which neglect the cross terms among propagators and invoke separate bath averages of propagators, differ from the exact results in Eq. (3.5).

Similarly, the photon-echo signal from the second-order cumulant expansion can be derived as

$$A_{\mathrm{echo}}(t_1,t_2)\approx e^{i\omega_0(t_2-t_1)}\exp(-2[\alpha_{11}(t_1)+\alpha_{22}(t_1)+\alpha_{11}(t_2)+\alpha_{22}(t_2)]), \quad (3.16)$$

where there is no contribution from pure dephasing. Again, this expression gives the correct expansion up to first order in bath fluctuations, thus is only applicable to weak solute-solvent interactions.

C. Markovian approximation

Under the Markovian approximation, the population relaxation profiles are given by $I_{n,\mathrm{pop}}(t)\approx\exp[-\mathrm{Re}(\Gamma_n)t]$. For the dissipative harmonic oscillator, Γ_n is given as

$$\Gamma_n=2\int_0^\infty\langle n|\langle V_{OD}(t)V_{OD}(0)\rangle_b|n\rangle dt =2\int_0^\infty\langle f(t)f(0)\rangle_b(e^{-i\omega_0 t}q_{n,n+1}^2+e^{i\omega_0 t}q_{n,n-1}^2)dt, \quad (3.17)$$

where $q_{n,n+1}=q_{n+1,n}=\sqrt{(n+1)\hbar/2\mu\omega_0}$ is the off-diagonal element of the position operator. In this limit, we readily work out the two population relaxation rates from the ground state and the first excited state, respectively, yielding

$$\Gamma_g=k_g=\frac{\gamma}{\omega_0^2+\gamma^2}\frac{\langle\delta f^2\rangle_b}{\mu\hbar\omega_0}, \quad \Gamma_e=k_e=\frac{\gamma}{\omega_0^2+\gamma^2}\frac{3\langle\delta f^2\rangle_b}{\mu\hbar\omega_0}. \quad (3.18)$$

Then, the average population relaxation rate is $k_{ge}=(k_g+k_e)/2$. It is straightforward to obtain the absorption profile and the echo signal at the Markovian limit,

$$A_{ge,\mathrm{abs}}(t)\approx e^{-i\omega_0 t}\exp\left[-\frac{\Gamma_g+\Gamma_e}{2}t\right], \quad A_{\mathrm{echo}}(t_1,t_2)\approx e^{i\omega_0(t_2-t_1)}\exp\left[-\frac{\langle\delta f^2\rangle_b}{\mu\hbar\omega_0}\frac{\gamma(t_1+t_2)}{\omega_0^2+\gamma^2}\right]. \quad (3.19)$$

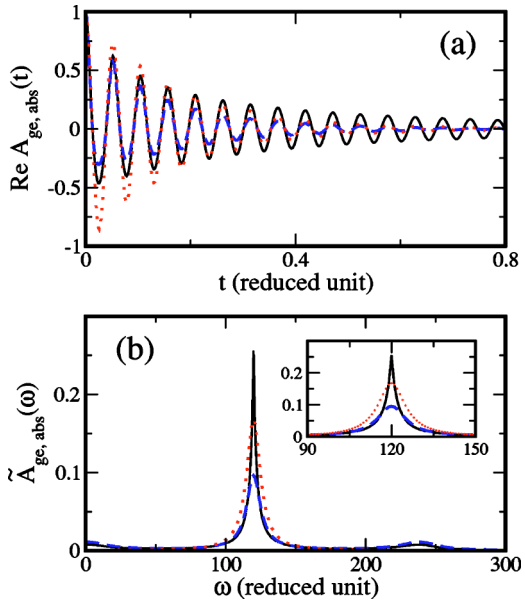

FIG. 1. Comparison of the temporal absorption profile of the dissipative harmonic oscillator calculated with the exact path integral expression in Eq. (3.4) (solid line), the second-order cumulant expansion in Eq. (3.13) (dashed line), and the Markovian approximation in Eq. (3.19) (dotted line). The corresponding frequency domain line shapes are given in the lower panel (b) with the details of the central peak in the inset. The parameters are $\omega_0=120$, $\gamma=10$, and $\langle \delta f^2\rangle_b=0.3\mu\hbar\omega_0^3$.

D. Numerical results and discussions

To demonstrate the differences between the nonperturbative and perturbative approaches, we calculate the vibrational line shapes for a dissipative harmonic oscillator described by the Hamiltonian in Eq. (3.1). The results are plotted in Figs. 1, 2, and 3. To facilitate the comparison with the Morse potential discussed in Sec. IV, we take the same frequency in reduced unit, $\omega_0=120$, and the same effective mass inreduced unit, $\mu=0.5$, which were used in simulations by Tuckerman, Bader, and Berne.[25,26] The effective $\hbar$ is 0.029 534. The friction kernel of the bath fluctuation is assumed to be single exponential, i. e., $\langle \delta f(t)\delta f(0)\rangle = \langle \delta f^2\rangle_b \exp[-\gamma|t|]$, which is a simplified description of environmental fluctuations. The decay rate $\gamma=10$ is 1/12 of the reduced frequency and the mean square fluctuation of the random force is $\langle \delta f^2\rangle=0.3\mu\hbar\omega_0^3$.

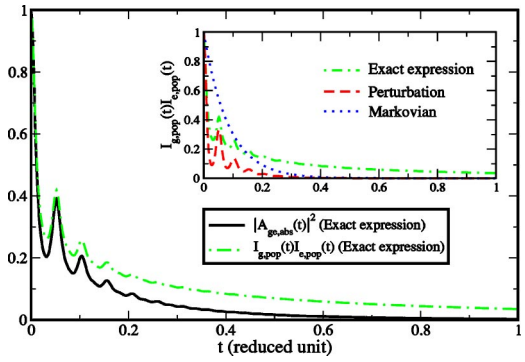

FIG. 2. Examination of the decomposition relation given by Eq. (2.13) with for the dissipative harmonic oscillator. The exact results, the cumulant expansion, and the Markovian approximation of the VER signal $I_{g,\mathrm{pop}}I_{e,\mathrm{pop}}$ are shown in the inset. The parameters are the same as in Fig. 1. For a linearly coupled harmonic oscillator, there is no pure dephasing, $|A_{ge,\mathrm{dep}}(t)|^2=1$.

1. Non-Markovian effects of VER

In Fig. 1, we illustrate the absorption profile $A_{ge,\mathrm{abs}}(t)$ and its Fourier transforms $A_{ge,\mathrm{abs}}(\omega)=\mathrm{Re}\int_0^\infty e^{i\omega t}A_{ge,\mathrm{abs}}(t)dt$ from the path integral method in Eq. (3.4), the second-order cumulant expansion in Eq. (3.13), and the Markovian approximation in Eq. (3.19). As indicated in Sec. III B, the perturbative and the exact results are identical up to first order in the bath fluctuation $\langle \delta f^2\rangle_b$. The perturbative approach only provides qualitative agreements and does not reproduce the line shape quantitatively. The Markovian approximation only captures the overall decay of the absorption profile. In the long-time limit, both perturbation and Markovian approximation yield exponential decaying envelops for the absorption amplitude with the decay rate $k_{ge}=(k_g+k_e)/2$, whereas the exact result gives a power-law decaying envelop of t^{-2} (see Sec. III A). Hence, the exact result is more coherent than the perturbative and the Markovian approximations. This difference becomes more prominent for stronger solute-solvent interactions.

As shown in Fig. 1, both the nonperturbative and the second-order cumulant expansion results have asymmetric envelops while the Markovian result is symmetric. This non-Markovian effect is an important feature of VER effects. To illustrate this point, we examine the second-order cumulant expansion expression for the population relaxation in Eq. (3.15). The exponent of the population relaxation profile is an incomplete Fourier transform of the friction kernel at the fundamental frequency, giving

$$2[\alpha_{11}(t)+\alpha_{22}(t)] = \frac{\langle \delta f^2\rangle_b}{2\mu\omega_0\hbar}\left[\frac{\omega_0^2-\gamma^2}{(\omega_0^2+\gamma^2)^2}+\frac{\gamma t}{\omega_0^2+\gamma^2} - \frac{(\omega_0^2-\gamma^2)\cos\,\omega_0 t-2\omega_0\gamma\,\sin\,\omega_0 t}{(\omega_0^2+\gamma^2)^2}e^{-\gamma t}\right]. \quad (3.20)$$

Equation (3.20) is intrinsically oscillatory with the fundamental frequency ω_0. As a result, the absorption amplitude is smaller on the negative side than on the positive side, generating an asymmetric temporal profile. Under the Markovian approximation, the exponent is simplified to be linear in time. Then, the oscillatory feature is completely removed, yielding a symmetric profile. Apparently the exponent is proportional to the mean square fluctuation of the bath, $\langle \delta f^2\rangle_b$, and the asymmetry is more prominent for stronger solute-solvent interactions.

The asymmetric feature is also demonstrated in the Fourier spectrum. The exact and the second-order cumulant expansion results show small side bands at zero frequency and the second harmonic frequency while the Markovian approximation is a perfect Lorentzian. These side bands are generated by the oscillations in the exponent. To illustrate this point, we further expand the perturbative expression of Eq. (3.13), yielding

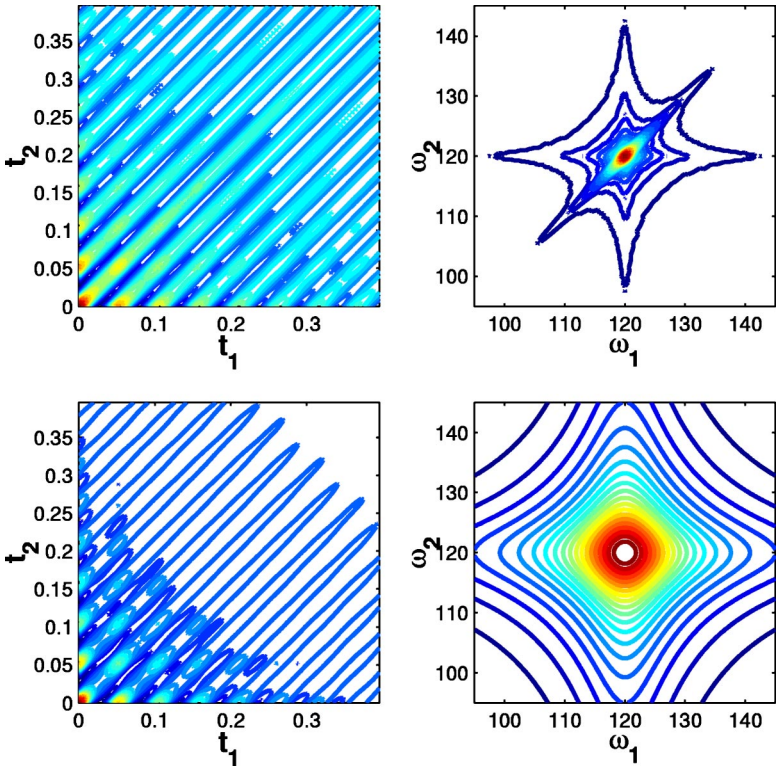

FIG. 3. The time-domain echo signals (in the left column) and their frequency domain contours (in the right column) for the dissipative harmonic oscillator. From top to bottom, the plots are the nonperturbative calculation and the second-order cumulant expansion, respectively. The parameters used in the calculations are the same as in Fig. 1.

$$A_{ge,\mathrm{abs}}(t)\approx e^{-i\omega_0 t}\exp\left[-\frac{2\langle\delta f^2\rangle_b(\omega_0^2-\gamma^2)}{\mu\omega_0\hbar(\omega_0^2+\gamma^2)^2}-\frac{\Gamma_g+\Gamma_e}{2}t\right]\times\sum_{n=0}^{\infty}\frac{(-1)^n}{n!}\left(\frac{\langle\delta f^2\rangle_b}{\mu\omega_0\hbar(\omega_0^2+\gamma^2)^2}e^{-\gamma t}\times[(-\omega_0^2+\gamma^2)\cos\,\omega_0 t-2\gamma\omega_0\sin\,\omega_0 t]\right)^n. \tag{3.21}$$

After collecting the Fourier components at zero, the first and the second harmonic frequencies, we identify several features in the absorption line shape, which are as follows:

(1) The central peak at ω_0 is a Lorentzian with width equal to the dephasing rate k_{ge}.

(2) The peaks at $\omega=0$ and $2\omega_0$ are slightly asymmetric with width $k_{ge}+\gamma$.

(3) In the limit $\omega_0\gg\gamma$, the ratio of the peak at $2\omega_0$ (or zero frequency) to the major peak at ω_0 is directly proportional to the dimensionless bath fluctuations

$$\frac{\tilde{A}(2\omega_0)}{\tilde{A}(\omega_0)}=\frac{\tilde{A}(0)}{\tilde{A}(\omega_0)}\approx\frac{\langle\delta f^2\rangle_b}{\mu\hbar\omega_0^3}\frac{k_{ge}}{k_{ge}+\gamma}. \tag{3.22}$$

The Markovian approximation neglects the constant term $-2\langle\delta f^2\rangle_b(\omega_0^2-\gamma^2)/\mu\omega_0\hbar(\omega_0^2+\gamma^2)^2$ in the exponent and generates a higher peak at $\omega=\omega_0$ than the second-order cumulant expansion. The quantitative relations in (1) and (2) provide a possible way to measure the two parameters, $\langle\delta f^2\rangle$ and γ, of the bath fluctuations.

2. Non-Lorentzian line shapes

Compared to the exact result of nonperturbative calculations, the absorption spectrum from the second-order cumulant expansion reproduces the line shapes at $\omega=0$, ω_0, and $2\omega_0$. Yet, the central peak of the exact spectrum at ω_0 is substantially different from a Lorentzian. Given the long-time power-law decay profile of the exact absorption profile, $A_{ge,\mathrm{abs}}(t)\approx e^{-i\omega_0 t}(1+\Gamma_{ge}t/2)^{-2}$ with $\Gamma_{ge}=k_{ge}$, the central peak is a Meijer G function and has a height of $2/k_{ge}$ and a width of $k_{ge}/2$. The non-Lorentzian absorption spectrum was also obtained by Kosloff and Rice from dynamical semigroup techniques that go beyond the weak coupling limit.[41] In their analysis, the non-Lorentzian peak is attributed to double quantum transition resulting from the quadratic system-bath coupling where both population and pure dephasing are present. Apparently, the dissipative harmonic oscillator discussed in the present paper is linearly coupled to the bath without pure dephasing contribution; hence, the non-Lorentzian shape we obtained results from couplings of population relaxations. This is a different interpretation of the absorption line shape.

The non-Lorentzian line shapes are also obtained in the photon-echo profile. Figure 3 is a comparison of the time-domain echo signals and their frequency domain line shapes. The two time-domain echo signals in the left column are obtained from the nonperturbative path integral method and the second-order cumulant expansion, respectively. The line

shapes in the right column are the corresponding absolute value spectra obtained from[34]

$$|A_{\mathrm{echo}}(\omega_1,\omega_2)| = \left| \int_0^\infty \int_0^\infty e^{i\omega_1 t_1 - i\omega_2 t_2} A_{\mathrm{echo}}(t_1,t_2)\, dt_1\, dt_2 \right|. \quad (3.23)$$

The second cumulant expansion has a symmetric 2D Lorentzian line shape and is almost identical to the Markovian line shape (not shown in Fig. 3). The close resemblance in the 2D Fourier spectra indicates the same long-time behavior for both approximations. The exact result, as shown in the absorption profile, decays in a power-law form of t^{-2} at long times. The Fourier spectrum shows a much wider distribution along the diagonal direction than the antidiagonal direction. In the dissipative harmonic oscillator we discussed here, the pure dephasing rate is zero, hence the elongated line shape along the diagonal direction can only result from population relaxation, which is different from the pure-dephasing-induced broadening discussed in the literature.[4] Compared to linear absorption spectrum, the nonlinear photon echo is much more sensitive to the nonperturbative effects.

3. Decomposition relation: Comparison of different approximations for VER

In Fig. 2, the decomposition relation in Eq. (2.13) is examined for the same parameter as those in Fig. 1. As we discussed in Sec. III A, the decomposition expression, obtained with the factorization approximation, is only accurate up to first order in $\langle \delta f^2 \rangle_b$ and overestimates the absorption intensity. This is clearly indicated by the deviation of $I_{n,\mathrm{pop}}(t) I_{n+1,\mathrm{pop}}(t)$ from $|A_{n,n+1,\mathrm{abs}}(t)|^2$. Compared to the exact result, the factorization approximation reproduces the short-time oscillations correctly and exhibits a slower decay profile in the long time. Hence, the composite approximation scheme of Eq. (2.19) in Sec. II B overestimates the absorption profile. The second-order cumulant expansion of the VER contribution derived in Eq. (3.15) clearly underestimates the absorption profile and decays faster than the exact result. The Markovian approximation is appropriate only for an estimation of the decay rate. Consequently, the composite approximation scheme of Eq. (2.23) reduces to the Markovian approximation in the absence of pure dephasing and fails to capture any non-Markovian features of VER. For the case of anharmonic potentials investigated later in Sec. IV, the pure-dephasing profile imposes a monotonic decaying envelop, where Eq. (2.19) agrees better with the exact result.

These calculations clearly demonstrate the limitations of the perturbative approach and the Markovian approximation. The perturbative expressions, which are obtained under the assumption of weak solute-solvent interactions, can provide a qualitative description of vibrational line shapes, but cannot accurately reproduce the details. The Markovian approximation oversimplifies the timedependence with simple relaxation rates and fails to capture the VER effects. That is why a more rigorous nonperturbative approach is important and necessary for studying vibrational line shapes in condensed phases.

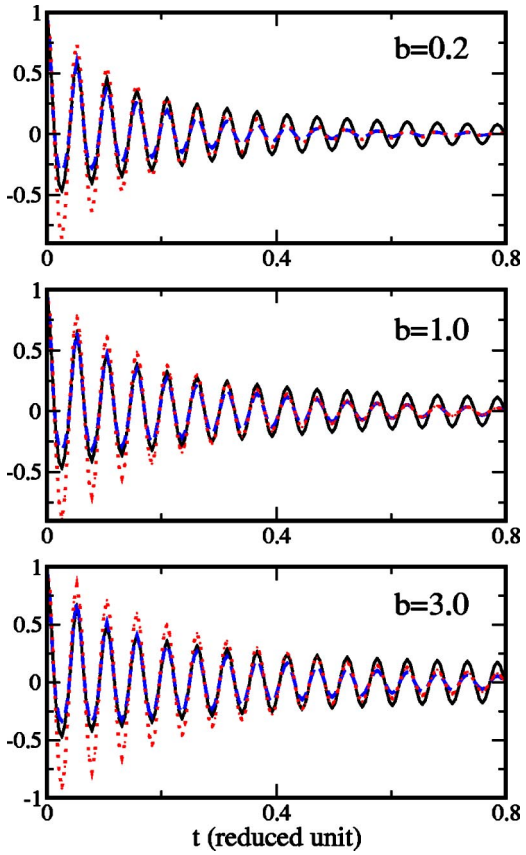

FIG. 4. Comparison of $\mathrm{Re}\, A_{ge,\mathrm{abs}}(t)$ calculated with the exact path integral expression (solid line), the second-order cumulant expansion (dashed line), and Markovian approximation (dotted line) for the dissipative harmonic oscillator coupled to a quantum Gaussian bath. $b=\beta\hbar\omega_0$ is the temperature parameter. The real part of the quantum force-force correlation is the same as in Fig. 1 and the imaginary part is given by $-i\tilde{C}_2(\omega) = \tanh(\beta\hbar\omega_0/2)\tilde{C}_1(\omega)$. The high temperature limit $\beta\hbar\omega_0 \to 0$ is Fig. 1(a).

E. Quantum bath

To demonstrate the quantum effects, we plot several absorption profiles in Fig. 4 and compare with the classical results. The details of the derivation are elaborated in Appendix B. Here we set the real part of the quantum force-force correlation equal to the classical force-force correlation function used in Fig. 1, i.e., $C_1(t) = \langle \delta f^2 \rangle_b \exp[-\gamma|t|]$, and assume the same parameters therein. The Fourier transform of $C_1(t)$ is $\tilde{C}_1(\omega) = 2\gamma\langle \delta f^2 \rangle_b / (\omega_0^2 + \gamma^2)$, and the imaginary part of the quantum force-force correlation function is determined from Eq. (B3),

$$C_2(t) = \frac{1}{\pi} \int_0^\infty \tanh \frac{\beta\hbar\omega_0}{2}\, \tilde{C}_1(\omega) \sin\, \omega t\, d\omega. \quad (3.24)$$

As shown in Fig. 4, the quantum absorption profiles are generally more coherent than the classical ones in the long-time limit and have weaker effects on the short-time profile. The perturbative approach yields closer resemblance to the exact result at lower temperatures. The asymmetry in the absorption profile from the vibrational energy relaxation remains prominent for quantum baths.

IV. DISSIPATIVE MORSE OSCILLATOR: A NUMERICAL EXAMPLE

Let us now consider a numerical example of anharmonic potentials and investigate the vibrational line shapes for a Morse oscillator linearly coupled to a Gaussian bath. The full Hamiltonian is given by

$$H=\frac{p^2}{2\mu}+D_e(1-e^{-\beta q})^2+f(t)q, \tag{4.1}$$

where D_e is the dissociation energy. Again the classical bath is represented by a Gaussian random force $f(t)$ and the bath relaxation is characterized by the friction kernel $C_{\rm cl}(t)=\langle f(t)f(0)\rangle_b$. For simplicity, we study the transition between the ground and first excited states. To facilitate the comparison with early studies in literature,[26] the Lennard-Jones fluid of Argon are used as the reference units with parameters $\epsilon/k_B=120$ K, $m=6.632\times10^{-26}$ Kg, and $\sigma=3.41$ Å. In these units, the dissociation energy is $D_e=207.36\epsilon=2.15$ eV. The diatomic molecule consists of two atoms with the same mass as Argon coupled by a Morse potential, giving the effective mass $\mu=0.5$ m$=20.0$ amu. $\beta=4.167\sigma^{-1}=1.22$ Å^{-1}, and the fundamental frequency $\omega_0=\sqrt{2D_e\beta^2/\mu}=120\sqrt{\epsilon/m\sigma^2}=296$ cm^{-1}. $\hbar$ in the reduced unit is $\hbar^*=\hbar(m\sigma^2\epsilon)^{-1/2}=0.029\,534$. To compare the nonperturbative and perturbative approaches, we calculate the vibrational line shapes for a solute-solvent interaction of $\langle\delta f^2\rangle_b=0.3\mu\hbar\omega_0^3$. The bath relaxation is an exponential $C_{\rm cl}(t)=\langle\delta f^2\rangle_b e^{-\gamma t}$ with $\gamma=10$.

The perturbative absorption profile with second-order cumulant expansion is given in Eq. (2.17), and the pure-dephasing and population relaxation cumulants are

$$g(t)=\frac{1}{\hbar^2}\int_0^t\int_0^\tau\langle\delta f(\tau)\delta f(\tau')\rangle_b(\langle q\rangle_{n+1}-\langle q\rangle_n)^2 d\tau\, d\tau', \tag{4.2}$$

$$h_n(t)=\frac{1}{\hbar^2}\int_0^t\int_0^\tau\langle\delta f(\tau)\delta f(\tau')\rangle_b \times\sum_{m\neq n}q_{nm}^2 e^{i\Omega_{mn}(\tau-\tau')}d\tau\, d\tau',$$

where q_{nm} is the matrix element of q. In the Markovian limit, Eq. (2.17) reduces to $A_{n,n+1,\rm abs}(t)\approx e^{-i\Omega_{n,n+1}t}\times\exp[-\Gamma'_{n,n+1}t-\frac{1}{2}(\Gamma_n+\Gamma_{n+1})t]$, where $\Gamma'_{n,n+1}$ and Γ_n are the pure-dephasing rate and the population relaxation rate given by

$$\Gamma'_{n,n+1}=\frac{(\langle q\rangle_{n+1}-\langle q\rangle_n)^2}{\hbar^2}\int_0^\infty\langle\delta f(\tau)\delta f(0)\rangle_b d\tau, \tag{4.3}$$

$$\Gamma_n=\sum_{m\neq n}\frac{2q_{nm}^2}{\hbar^2}\int_0^\infty\langle\delta f(\tau)\delta f(0)\rangle_b e^{i\Omega_{mn}\tau}d\tau.$$

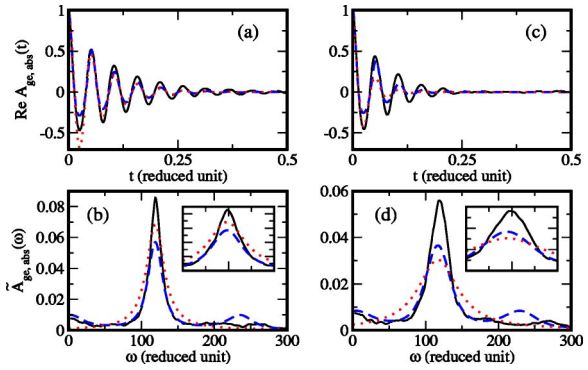

FIG. 5. Absorption line shapes of the dissipative Morse oscillator calculated with the nonperturbative method (solid line), the second-order cumulant expansion (dashed line), and the Markovian approximation (dotted line). The solvent relaxation rate is assumed to be $\gamma=10$. The solute-solvent interaction is $\langle\delta f^2\rangle_b=0.3\mu\hbar\omega_0^3$. At anharmonicity $\chi_e=0.004\,27$ in (a) and (b), the dissociation threshold is $D_e=58.5\omega_0$ and the fundamental frequency $\omega_0=120$. At anharmonicity $3\chi_e$ in (c) and (d), the dissociation energy is $D_e/3$ but μ and ω_0 remain the same.

A. Asymmetric envelops in the temporal absorption profile

As shown in Fig. 5(a), the second-order cumulant expansion illustrates the presence of asymmetric signals at short times but fails to reproduce the long-time decaying envelop. Similar to the dissipative harmonic oscillator studied in Sec. III, the appearance of asymmetry in the absorption profile clearly demonstrates the VER effects from the off-diagonal elements of the solute-solvent interaction. For the exponential frictional kernel, $g(t)$ and $h_n(t)$ are evaluated explicitly as

$$g(t)=\frac{\langle\delta f^2\rangle_b}{\hbar^2}(q_{n+1,n+1}-q_{nn})^2\frac{\gamma t-1+e^{-\gamma t}}{\gamma^2},$$

$$h_n(t)=\frac{\langle\delta f^2\rangle_b}{\hbar^2}\sum_{m\neq n}q_{nm}^2\left[\frac{\Omega_{mn}^2-\gamma^2}{(\Omega_{mn}^2+\gamma^2)^2}+\frac{\gamma t}{\Omega_{mn}^2+\gamma^2}-\frac{(\Omega_{mn}^2-\gamma^2)\cos\,\Omega_{mn}t-2\Omega_{mn}\gamma\,\sin\,\Omega_{mn}t}{(\Omega_{mn}^2+\gamma^2)^2}e^{-\gamma t}\right]. \tag{4.4}$$

According to Eq. (4.4), the pure-dephasing profile decays monotonically while the VER profile is an oscillatory function. The bath relaxation rate is significantly smaller than the energy gap, i.e., $\gamma\ll\omega_0$, and the vibrational energy gap falls far into the tail of the spectral density of bath relaxation. The pure-dephasing rate is equivalent to a Fourier transform with zero frequency and is located at the center of the spectral density of bath relaxation. Consequently, the pure-dephasing rate is much larger than the population relaxation rate in the long-time limit. At short times, $h_n(t)+h_{n+1}(t)\gg g(t)$; hence, the VER dominates at short times and the asymmetric envelop becomes more prominent. The Markovian approximation employs simple rate approximation and completely removes the oscillatory feature in population relaxation and produces a symmetric profile over the complete time range.

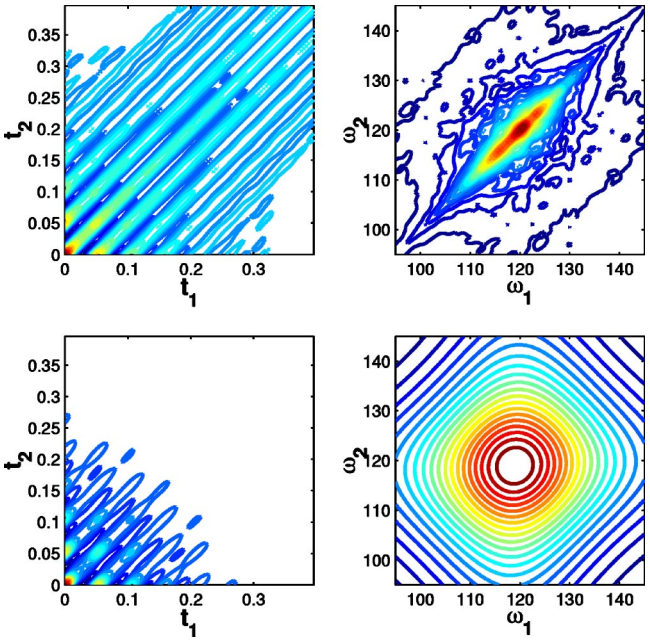

FIG. 6. The time-domain echo signals (in the left column) and their frequency domain contours (in the right column) for the dissipative Morse oscillator. From top to bottom, the plots are the nonperturbative calculation and the second-order cumulant expansion, respectively. The parameters used in the calculations are the same as in Figs. 5(a) and 5(b).

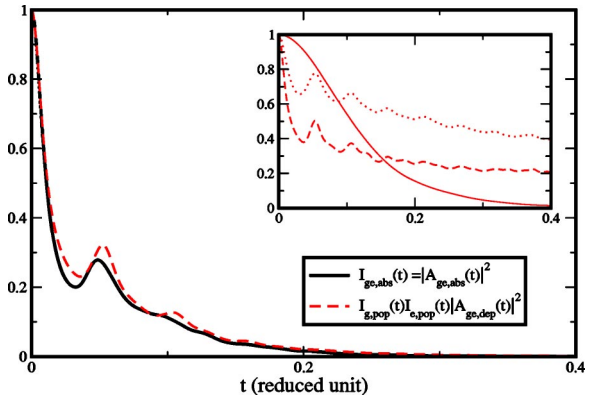

FIG. 7. Examination of the decomposition relation in Eq. (2.13) for the dissipative Morse potential. Inset: The decomposed signals $I_{g,\mathrm{pop}}(t)$ (dotted line), $I_{e,\mathrm{pop}}(t)$ (dashed line), and $|A_{ge,\mathrm{dep}}(t)|^2$ (solid line). $A_{ge,\mathrm{abs}}(t)$, $I_{g,\mathrm{pop}}(t)$, and $I_{e,\mathrm{pop}}(t)$ are the exact results calculated numerically with the same parameters as those in Figs. 5(a) and 5(b).

The absorption spectrum of the Markovian approximation illustrated in Fig. 5(b) has a symmetric Lorentzian line shape from the simple rate approximation. The perturbation renders side bands at zero and the second harmonic frequencies in addition to the central peak. This is a direct result of the asymmetric VER signal at short times. The side bands are solvent-induced multiple-photon transitions which are absent in the Markovian VER treatment. Apparently, the exact result has a non-Lorentzian central peak, differing from the Markovian approximation. Yet, the non-Lorentzian central peak is not as sharp as that of a dissipative harmonic oscillator in Fig. 1. This difference results from the dominant contribution of pure dephasing, which is absent in a harmonic oscillator. Pure-dephasing profile, when superimposed onto population relaxation profile, generates an exponentially decaying envelop in the long time and results in a less sharp non-Lorentzian peak.

B. Asymmetric central peak in absorption spectrum

In addition to the nonLorentzian peak and side bands, the nonperturbative calculation demonstrates an asymmetric central peak in frequency domain. Absence of these features from the perturbative and Markovian approximations indicates that they arise from neglected term in the factorization of perturbative approach. Careful investigation of the approximations in Sec. II B reveals that the source of this asymmetry is the cross products of the off-diagonal coupling, $\langle\langle V_{\mathrm{OD}}(t_1)V_{\mathrm{OD}}(t_2)\rangle_n\langle V_{\mathrm{OD}}(t_1)V_{\mathrm{OD}}(t_2)\rangle_{n+1}\rangle_b$. For an anharmonic potential, the frequency gaps Ω_{mn} are not identical, the frequency mismatch generates a complex envelop function, while the negligence of cross products in the perturbative and the Markovian approximations only yields a real envelop. The presence of the imaginary part of the envelop function creates interferences of difference frequency components, giving an asymmetric profile. As anharmonicity increases, the frequency mismatch becomes larger and thus the interference becomes stronger, yielding more asymmetric central peaks, as shown in Fig. 5(d). Apparently, the cross product of the off-diagonal coupling is proportional to $\langle\delta f^2\rangle_b^2$ and depends strongly on the strength of bath fluctuations. In Sec. V, the O–H stretch has a much weaker coupling to the bath than the Morse oscillator calculated in this section and demonstrates a less prominent asymmetric absorption spectrum.

The asymmetric and non-Lorentzian line shape is better manifested in the nonlinear two-pulse photon-echo (2PE) profile. As shown in Fig. 6, the exact result shows a strong asymmetric elongation along the diagonal and is significantly different from the Lorentzian line shape predicted by the second-order cumulant expansion and the Markovian approximations. The Markovian approximation has identical line shapes as the second-order cumulant expansion and is not included here to avoid redundancy. Small irregular structures in the exact line shape is due to insufficient averaging in Monte Carlo simulation.

C. Decomposition relation: Anharmonic effects

To check the decomposition relation, we calculate $I_{ge,\mathrm{abs}}(t)=|A_{ge,\mathrm{abs}}(t)|^2$ and compare it with the product of $I_{g,\mathrm{abs}}(t)$, $I_{e,\mathrm{abs}}(t)$ and $|A_{ge,\mathrm{dep}}(t)|^2$. Due to the presence of anharmonicity, the absorption profile is dominated by pure dephasing in the long time limit, so that the factorization result yields close resemblance to the nonperturbative absorption profile, displayed in Fig. 7. The initial decay, the major oscillation at $t\approx 0.05$, and the long-time relaxation are closely predicted by the factorization scheme. The similarity between the absorption intensity and the decomposed signal

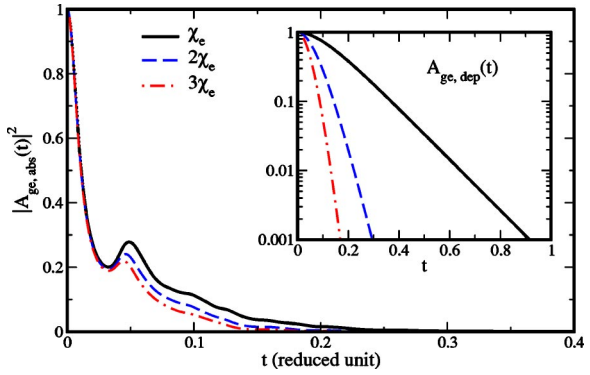

FIG. 8. The nonperturbative absorption amplitude $|A_{ge,\mathrm{abs}}(t)|^2$ and the pure-dephasing profile $A_{ge,\mathrm{dep}}(t)$ for different anharmonicities of a dissipative Morse potential. Other parameters such as ω_0, μ, γ, and $\langle \delta f^2 \rangle_b$ remain the same as previous calculations.

indicates the applicability of the approximation scheme of Eq. (2.19) introduced in Sec. II D, which directly superimposes the population relaxation profile measured from pump-probe experiments onto the pure-dephasing profile. This approach is different from the cumulant approximation where both the population relaxation and the pure dephasing are truncated at the second-order cumulant. Consequently, the absorption spectrum is no longer a Lorentzian shape. As we discussed earlier in Sec. II D, due to the omission of imaginary part of the population relaxation signal, the composite approximation scheme cannot reproduce the asymmetric central peak of the absorption spectrum.

To investigate the anharmonic effects, we compare the absorption intensity and the pure-dephasing signal at $\chi_e = \hbar\omega_0/4D_e$, $2\chi_e$ and $3\chi_e$ in Fig. 8 with ω_0 and μ fixed. The position operator q of a Morse oscillator is[50,51]

$$q \approx -\frac{1}{\beta}\ln[1-\sqrt{\chi_e}(b+b^\dagger)]$$

$$\approx \frac{\hbar}{2\mu\omega_0}[(b+b^\dagger)+\sqrt{\chi_e}(b+b^\dagger)^2], \tag{4.5}$$

where b and $b^\dagger$ are the creation and annihilation operators of the Morse oscillator, respectively, and $\chi_e = [8D_e\mu/(\hbar^2\beta^2)]^{-1/2}$ is the anharmonicity parameter. The spectrum of the Morse oscillator is $E_n = \hbar\omega_0[(n+1/2) - \chi_e(n+1/2)^2]$, with $1/(2\chi_e)$ the number of bounded states in the potential well. For the Morse oscillator discussed here, $\chi_e \approx 0.004\,27$. The population relaxation rate is much smaller than the pure-dephasing rate due to the large difference between the frequency gap and the bath relaxation rate. Furthermore, the ratio between V_D and V_{OD} is proportional to $\sqrt{\chi_e}$. With increasing anharmonicity, the contribution from pure dephasing becomes dominant; hence, the short-time oscillatory feature from the population relaxation is further suppressed and the absorption profile decays faster.

D. VER effects as a function of anharmonicity

We now examine the different perturbation schemes of VER and compare the absorption profiles at three different anharmonicities, χ_e, $2\chi_e$, and $3\chi_e$ in Fig. 9. The approxi-

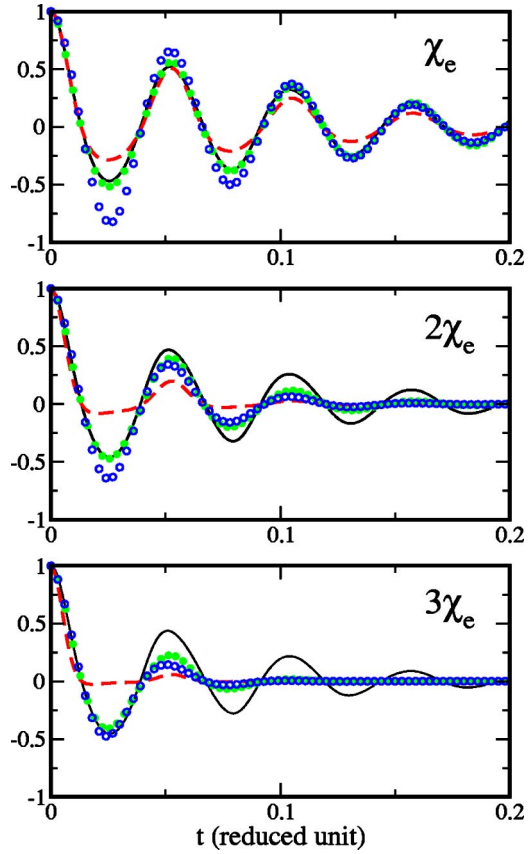

FIG. 9. Comparison of the nonperturbative calculation in Eq. (2.3), the second-order cumulant expansion in Eq. (2.17), and the two composite approximation schemes in Eqs. (2.19) and (2.23) at different anharmonicities. Other parameters such as ω_0, μ, γ, and $\langle \delta f^2 \rangle_b$ remain the same as previous calculations. The exact results of the nonperturbative calculation are plotted in solid lines, the second-order cumulant expansion in dashed lines, Eq. (2.19) in solid circles, and Eq. (2.23) in open circles.

mations employed in the second order cumulant expansion include decoupling of the diagonal V_D and the off-diagonal V_{OD}, independent bath averages of propagators, and cumulant expansion, which are discussed in detail in Secs. II B and III B. The factorization propagator in Eq. (2.10) neglects the commutator between $V_D(t)$ and $V_{\mathrm{OD}}(t)$. For the linear coupling, the commutator can be estimated explicitly as

$$[V_D(\tau), V_{\mathrm{OD}}(\tau')] \propto f(\tau)f(\tau')\frac{\hbar}{2\mu\omega_0}\sqrt{\chi_e} \tag{4.6}$$

and is proportional to the square root of the anharmonicity. The negligence of this term significantly reduces the accuracy of the perturbative approximation at large anharmonicities. Furthermore, the commutator term includes the off-diagonal coupling and is oscillatory. Similar to the population relaxation term, the commutator term contributes significantly at short times and the contribution increases with anharmonicity. The nonperturbative signal, which includes the commutator $[V_D(t), V_{\mathrm{OD}}(t)]$ and cross terms between different propagators, is generally more coherent than the perturbative approximations. The difference between the nonperturbative and the perturbative results becomes more prominent at larger anharmonicities.

TABLE I. Relevant parameters of several VER systems.

	O–H[a]	O–D[b]	I_2[c]	C–O stretch[d]	HbCOl[e]	HgI[f]
Fundamental Ω_{01} (cm^{-1})	3400	2500	210.9	1714.4	1950	125
Overtone Ω_{12} (cm^{-1})	3150	2350	207.2	1706.3	1924	⋯
Bath fluctuation $\langle \delta f^2 \rangle_b / (\mu \hbar \omega_0^3)$	0.0162	0.0148	0.0313	0.064	0.029	0.068
γ_1^{-1} (fs)	~60	~30	~2500	3.4	500	65
γ_2^{-1} (fs)	~1200	~500	⋯	100	1200	⋯

[a]O–H stretch in liquid D_2O in Refs. 52 and 55. $\langle \delta f^2 \rangle_b$ is extracted from frequency gap fluctuations.
[b]O–D stretch in liquid H_2O in Ref. 56. $\langle \delta f^2 \rangle_b$ is extracted from force-force correlation function simulation.
[c]I_2 in Xenon solvent at 313 K and 3.0 g/cm^3 in Ref. 16. $\langle \delta f^2 \rangle_b$ is from force-force correlation function simulation.
[d]CH_3CO_2H cyclic dimer in CCl_4 solvent from Ref. 58. $\langle \delta f^2 \rangle_b$ is extracted from frequency gap fluctuation measurements.
[e]Carbon monoxide hemoglobin in D_2O solvent from Ref. 59. $\langle \delta f^2 \rangle_b$ is extracted from vibrational relaxation rate measurements.
[f]HgI in ethanol from Ref. 60. $\langle \delta f^2 \rangle_b$ is extracted from force-force correlation function simulation.

The composite approximation of Eq. (2.19) superimposes the population relaxation profile from pump-probe experiments onto the pure dephasing and accurately reproduces the asymmetric temporal profile at small anharmonicities. With increasing anharmonicity, the cross products of the off-diagonal couplings and diagonal couplings neglected from the decomposition in Eq. (2.19) contribute substantially to absorption profile. Hence, the deviation from the exact result increases with anharmonicity. The composite approximation of Eq. (2.23) assumes a Markovian rate for VER and yields a symmetric absorption profile. For the anharmonicities we studied, Eq. (2.23) does not work as well as Eq. (2.19). The strong deviations of the approximation schemes from the exact result at large anharmonicities justify the need for the nonperturbative treatment of vibrational line shapes.

V. O–H STRETCH IN D_2O ENVIRONMENTS

Now we demonstrate the importance of VER effects in a real system. The parameters of several VER systems are estimated and listed in Table I. The dimensionless bath fluctuation is estimated from simulations and frequency gap fluctuations assuming a Morse potential and a linear system-bath coupling. Although real systems include vibration-rotation couplings, intermolecular couplings, and other effects, the linear coupling assumed in our model still serves as a quantitative estimation of the VER effects. To illustrate the detailed contributions from VER, we perform a series of calculations for the O–H stretch in D_2O environment. The effective Hamiltonian is assumed to be the same as Eq. (4.1) and includes a Morse oscillator linearly coupled to a Gaussian classical bath. The electronic field experienced by the O–H stretch in the hydrogen-bond network is found to follow underdamped motion by computer simulations,[19–22] photon-echo spectroscopy,[52] and other ultrafast infrared (IR) measurements.[53–55] It is shown in the literature[19–22,52–57] that the relaxation time is about 30–170 fs in the short-time profile while the characteristic time of the long-time decay is roughly 0.5–2.0 ps. The two different time scales of the frictional kernel arise from a hydrogen-bond stretching at short times and a collective relaxation at long times. The ratio of the short-time relaxation rate to the O–H stretch frequency (~3430 cm^{-1}) is roughly 0.01–0.05. The dimensionless bath fluctuation amplitude estimated from simulations and experiments[19–22,55] is $\langle \delta f^2 \rangle_b / (\mu \hbar \omega_0^3) \approx 1.22 \times 10^{-2}$. For simplicity, we choose a biexponential friction kernel to reflect the two time scales, i.e., $\langle \delta f(\tau) \delta f(0) \rangle_b = \langle \delta f^2 \rangle_b [p e^{-\gamma_1 t} + (1-p) e^{-\gamma_2 t}]$, where $\gamma_1^{-1} = 40$ fs and $\gamma_2^{-1} = 600$ fs. The dissociation energy D_e and β are obtained from the literature[61] and the parameter are summarized in Table II. Given the Morse parameters, the number of the bounded states in O–H bond is estimated to be 22, and the anharmonicity parameter is $\chi_e \approx 0.0217$.

A. Solute-solvent coupling

The second-order cumulant expansion yields almost identical temporal absorption profiles as the nonperturbative calculation due to the weak bath fluctuations and the asymmetric envelop from non-Markovian VER effects is rather weak. On the other hand, the Markovian approximation assumes fast relaxation of bath and is only applicable to the long-time limit when $t \gg \gamma_1^{-1}, \gamma_2^{-1}$. The presence of the slow relaxation in the friction kernel violates this assumption; consequently, the Markovian approximation overestimates the decay rate substantially and deviates significantly from both the nonperturbative and the perturbative calculations. These findings are illustrated in Fig. 10(a). In Fourier space, the weakly asymmetric envelop of the absorption profile is reflected in the weak side bands of absorption spectrum. The side bands are generated by the solvent-induced multiple-photon transitions and non-Markovian VER treatment.

For the O–H bond, the anharmonicity parameter χ_e is as large as 0.0217. This is about 50 times larger than the Morse

TABLE II. Parameters of O–H stretch. The parameters of O–H stretch are taken from Ref. 61 and the D_2O environmental parameters γ_1, γ_2, and $\langle \delta f^2 \rangle_b$ are estimated from literature (Refs. 19–22 and 55).

D	8.84×10^{-12} erg
β	2.175×10^8 cm^{-1}
μ	1.66×10^{-24} g
ω_0	7.2916×10^{14} s^{-1}
γ_1^{-1}	40 fs
γ_2^{-1}	600 fs
p	0.8
$\langle \delta f^2 \rangle_b / \mu \hbar \omega_0^3$	0.0122

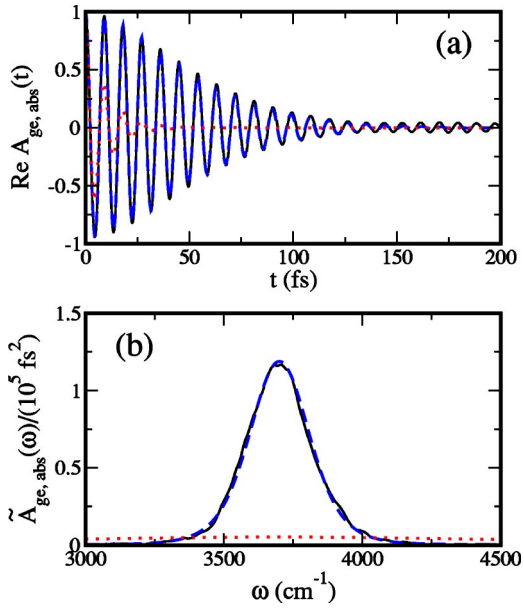

FIG. 10. Comparison of the nonperturbative calculation, the second-order cumulant expansion, and the Markovian approximations for the O–H stretch in D_2O network. The parameters are summarized in Table II. The exact results of the nonperturbative calculation are plotted in solid lines, the second-order cumulant expansion results in dashed lines, and the Markovian approximation in dotted lines.

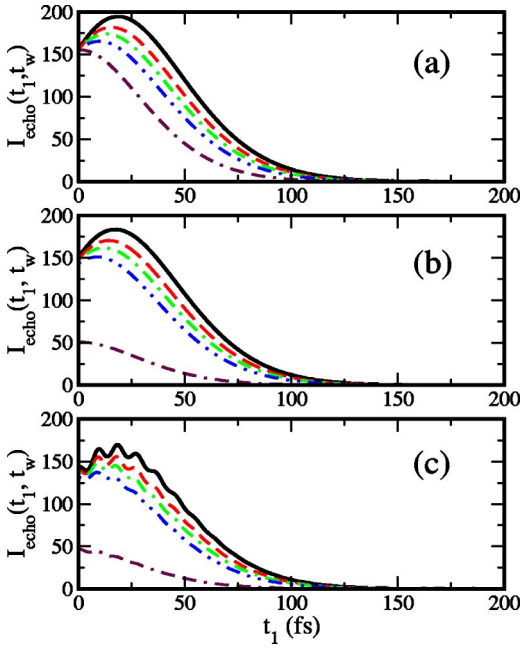

FIG. 11. Comparison of the perturbative calculations of the echo intensity $I_{\mathrm{echo}}(t_1,t_w)$ (a) without VER, (b) with Markovian VER, and (c) with cumulant approximation of VER. The waiting time t_w is varied, from top to bottom, $t_w=0,10,20,40,1000$ fs. The unit of $I_{\mathrm{echo}}(t_1,t_w)$ is fs.

potential discussed in Sec. IV. The dimensionless bath fluctuation is about 25 times smaller than that in Sec. IV. Due to these two effects, a weakly asymmetric central peak of the absorption spectrum compared to Fig. 5 is observed and the perturbation result reproduces the absorption spectrum quite accurately.

B. VER effects in 3PEPS measurements

In the 3PEPS experiment, the integrated photon-echo signal is collected and the photon-echo peak shift is determined as a function of the intermediate waiting time t_w.[4,7,8,55] For the purpose of illustration, we consider the same excitation path way discussed in Sec. II A. Assuming δ-function pulses, we derive the 3PE amplitude as

$$\begin{aligned} A_{\mathrm{echo}}(t_1,t_w,t_2)=&\langle\langle e^{-iH(t_w+t_2)}\rangle_{n+1}\langle e^{-iHt_1}\rangle_n\langle e^{-iHt_2}\rangle_n^\dagger \\ &\times\langle e^{-iH(t_1+t_w)}\rangle_{n+1}^\dagger\rangle_b \\ &+\langle\langle e^{-iHt_2}\rangle_{n+1}\langle e^{-iH(t_1+t_w)}\rangle_n \\ &\times\langle e^{-iH(t_w+t_2)}\rangle_n^\dagger\langle e^{-iHt_1}\rangle_{n+1}^\dagger\rangle_b . \end{aligned} \tag{5.1}$$

The integrated photon-echo signal is $I_{\mathrm{echo}}(t_1,t_w)=\int_0^\infty|A_{\mathrm{echo}}(t_1,t_w,t_2)|^2dt_2$. t_1 is the dephasing time between the first pulse and the second pulse, t_w is the waiting time between the second and the third pulses, and t_2 is the rephasing time between the third and the probe pulses. Following the same perturbation scheme discussed in Sec. III B, we separate pure dephasing from the diagonal coupling and VER from the off-diagonal coupling. The echo signal $A_{\mathrm{echo}}(t_1,t_w,t_2)$ is given by

$$\begin{aligned} &A_{\mathrm{echo}}(t_1,t_w,t_2) \\ &\approx e^{-\Omega_{n,n+1}(t_2-t_1)}(\exp[-h_{n+1}^*(t_1+t_w)-h_n^*(t_2) \\ &\quad -h_{n+1}(t_w+t_2)-h_n(t_1)]+\exp[-h_{n+1}^*(t_1) \\ &\quad -h_n^*(t_w+t_2)-h_{n+1}(t_2)-h_n(t_1+t_w)]) \\ &\quad\times\exp[-g^*(t_1)+g(t_w)-g^*(t_2)-g^*(t_1+t_w) \\ &\quad -g(t_w+t_2)+g^*(t_1+t_w+t_2)], \end{aligned} \tag{5.2}$$

where $g(t)$ is the line shape function and $h_n(t)$ characterizes the population relaxation contribution from the nth vibrational state. In the limit $t_w=0$, Eq. (5.2) reduces to the 2PE expression in Eq. (2.18). If the off-diagonal solute-solvent interaction is negligible compared to the pure dephasing, i.e., $h_n(t)\approx 0$, Eq. (5.2) reduces to the well-known result of three-pulse photon-echo response function for a two-level system.[4,7]

In Fig. 11, we plot the integrated photon-echo signal $I_{\mathrm{echo}}(t_1,t_w)=\int_0^\infty|A_{\mathrm{echo}}(t_1,t_w,t_2)|^2dt_2$ without VER, with the Markovian VER rate, and with the cumulant approximation of VER, respectively. Perturbative calculations are sufficiently accurate here due to weak bath fluctuations. In Eq. (5.2), the pure-dephasing terms containing t_w cancel out at large t_w and $I_{\mathrm{echo}}(t_1,t_w)$ reaches a stable nonzero function of t_1 without VER, as shown in Fig. 11(a). VER essentially decreases the signal amplitude during the waiting time t_w. At short waiting times, the cumulant approximation of VER imposes small oscillation onto the integrated echo intensity, yet does not affect the overall shape of the integrated photon-echo signal. The average population relaxation time is estimated to be $(k_g+k_e)^{-1}\approx 850$ fs. At large t_w, the echo in-

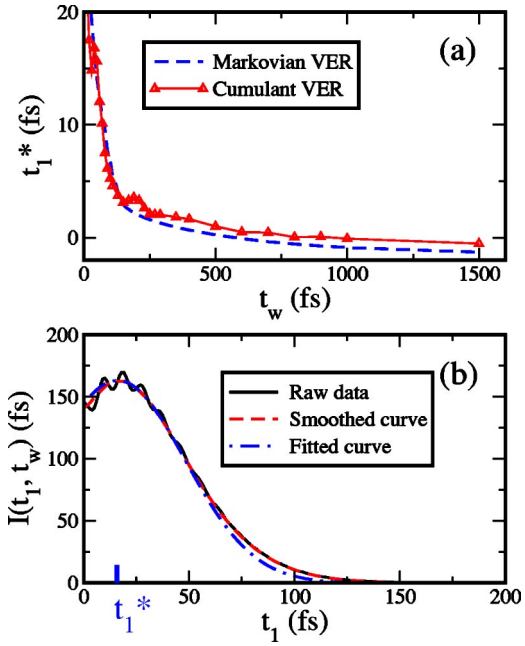

FIG. 12. (a) Comparison of the echo shifts with Markovian VER and with cumulant VER (triangles). $I_{\mathrm{echo}}(t_1,t_w)$ is first smoothed with a sliding window average of 10 fs, and the peak shifts are then determined with Gaussian fitting. (b) Determination of the peak shift t_1^*.

tensity approaches zero with population relaxation, as shown in Figs. 11(b) and 11(c), which is completely different from the case where VER is not accounted.

A nontrivial VER contribution is demonstrated in the peak shifts of integrated echo signal. Considering the experimental resolutions, we compute the integrated echo signal with a sliding window average of 10 fs and fit $I_{\mathrm{echo}}(t_1,t_w)$ with a Gaussian function, as shown in Fig. 12(b). It is clear in Fig. 12(a) that the peak shifts demonstrate different time scales and the peak-shift amplitude decreases due to the VER effects. The perturbation calculation with second-order cumulant expansion yields small recurrence around 200 fs, which corresponds to the frequency difference of the fundamental and the overtone $\Omega_{12}-\Omega_{01}\sim 250\ \mathrm{cm}^{-1}$. The recurrence cannot be reproduced with VER rates and therefore is a clear indication of non-Markovian VER effects. The experimentally observed recurrence at 150–170 fs includes additional contributions from the the underdamped frictional kernel.[55] The small oscillation around 40 fs is attributed to insufficient average from the narrow sliding window of 10 fs and Gaussian fitting errors. Compared to the linear absorption spectrum, the nonlinear 3PEPS is a more sensitive probe of the anharmonic effects.

VI. CONCLUSIONS

Nonperturbative and perturbative approaches are applied to vibrational line shape calculations. The nonperturbative approach based on Feynman's path integral formalism directly evaluates the quantum propagator in the interaction picture. In the perturbative approach, the solute-solvent interaction is first decomposed into diagonal and off-diagonal elements and the absorption profile is factorized into two parts: the population relaxation profile related to the off-diagonal coupling and the pure-dephasing profile related to the diagonal coupling. This factorization scheme neglects the commutator between the diagonal and the off-diagonal coupling, an important contribution which increases with anharmonicity. In the factorization scheme, we evaluate the bath average for each propagator separately and obtain the decomposition relation $A_{\mathrm{abs}}(t)\approx e^{i\Omega_{n,n+1}t}\sqrt{I_{n,\mathrm{pop}}(t)I_{n+1,\mathrm{pop}}(t)}A_{n,n+1,\mathrm{dep}}(t)$. Next, we apply the second-order cumulant expansion to the decomposition relation and derive the line shape function $g(t)$ and the population relaxation function $h_n(t)$. The approximation scheme of Eq. (2.19) directly superimposes the population relaxation profile from pump-probe experiments onto the pure-dephasing profile and can reproduce the asymmetric absorption profile. The approximation scheme of Eq. (2.23) treats population relaxation with the corresponding Markovian limit while evaluating the pure dephasing at the second-order cumulant. Due to the Markovian approximation to VER, Eq. (2.23) gives a symmetric absorption profile without side bands in the absorption spectrum. In the VER rate description, the solvent relaxation is much slower than the vibrational frequency gap and the line shapes are dominated by pure dephasing. On the other hand, the Markovian treatment of the VER contribution to line shapes requires a fast bath relaxation which results in the inconsistency of the Markovian VER rate. Finally, in the Markovian limit, the decomposition relation recovers the well-known relation among the vibrational dephasing rate, the population relaxation rate, and the pure-dephasing rate.

Analytical solutions for a dissipative harmonic oscillator yield quantitative estimation of the errors for different approximation schemes. $I_{g,\mathrm{pop}}(t)I_{e,\mathrm{pop}}(t)$ differs from $|A_{ge,\mathrm{abs}}(t)|^2$ at second order of bath fluctuations $\langle\delta f^2\rangle_b/(\mu\hbar\omega_0^3)$. Consequently, the decomposition in Eq. (2.13) is valid for weak solute-solvent interactions and becomes less accurate for strong solute-solvent interactions or for vibrational relaxation systems with small frequency gaps. We also show that the approximation scheme of Eq. (2.19) overestimates while the second-order cumulant expansion always underestimates the effects of friction. For the dissipative harmonic potential, non-Markovian VER effects generate asymmetric envelops in the time-domain absorption profile and side bands in the frequency domain absorption spectrum. The side bands are solvent-induced multiple-photon transitions and are absent in the Markovian VER treatment. The non-Lorentzian peak in nonperturbative treatments of absorption spectrum arises from couplings of population relaxations from different vibrational states. The nonperturbative VER effects manifest as a non-Lorentzian broadening along the diagonal direction in the frequency domain photon-echo spectra. Quantum baths have more coherence in the long-time profile but show less effects on the short-time profile and the coherence decreases with increasing temperature.

For the dissipative Morse potential, the interference of population relaxations from different vibrational states leads to an asymmetric central peak in the absorption spectrum with the asymmetry increasing with anharmonicity. The second-order cumulant expansion and the Markovian ap-

proximation result in a symmetric Lorentzian spectrum but can not reproduce vibrational line shapes correctly. When the frequency gap is much larger than the bath relaxation rate, pure dephasing dominates over population relaxation. In addition, the ratio between the diagonal coupling and the off-diagonal coupling is proportional to the square root of anharmonicity; therefore, the contribution from pure dephasing becomes dominant at large anharmonicities. All the three approximation schemes, the second-order cumulant expansion, the composite schemes of Eqs. (2.19) and (2.23), neglect the cross terms of population relaxations from different vibrational states and the cross terms between V_D and V_{OD}, and deviate significantly from exact results at large anharmonicities. Relatively speaking, Eq. (2.19) is better than Eq. (2.23) for all the anharmonicities we study.

For an O–H stretch in hydrogen-bond environments, the Markovian approximation substantially overestimates the decay rate from slow bath relaxation and results in significant deviation from both the nonperturbative and the perturbative calculations. Three-pulse photon-echo peak shift (3PEPS) measurement provides a more sensitive nonlinear probe of the VER effects. In these experiments, both the integrated 3PE signal amplitude and the echo peak shifts become smaller due to VER effects. More importantly, the non-Markovian VER effects generate a small recurrence around 200 fs. This recurrence corresponds to the frequency difference of the fundamental Ω_{01} and the overtone Ω_{12}, a result that cannot be reproduced by the Markovian VER rate. In general, nonlinear spectroscopic measurements such as two-pulse and three-pulse IR photon echos are more sensitive to the nonperturbative and non-Markovian VER effects than linear absorption.

The nonperturbative approach proposed in this paper treats the solute-solvent interaction accurately. Combined with the explicit treatment of the solvent degree of freedom, the nonperturbative propagation method provides a numerical tool to calculate the vibrational spectrum in condensed phases. The various perturbation schemes allow us to analyze contributions from different relaxation mechanisms and compare information contents from different spectroscopic measurements. In particular, the second-order cumulant expressions with both the pure-dephasing moment $g(t)$ and the VER moment $h_n(t)$ capture the essential features of vibrational line shapes for most realistic systems. The nonperturbative approach is essential for quantitative comparison with experimental measurements in systems with strong dissipative or non-Gaussian environments.

ACKNOWLEDGMENTS

This research was supported by the NSF Career Award (Grant No. Che-0093210) and the Petroleum Research Fund administrated by the American Chemical Society. J. C. is a recipient of the Camille Dreyfus Teacher-Scholar Award. The authors are grateful to Professor Robert Silbey and Professor Andrei Tokmakoff for stimulating discussions.

APPENDIX A: ANHARMONICITY-INDUCED DEPHASING

We now explore the molecular origin of pure dephasing. Taylor expansion of the solute-solvent interaction leads to

$$V(q-x)=V(q)+(a+a^+)f(x)+\tfrac{1}{2}(aa^+ +a^+a)e(x)+\cdots . \tag{A1}$$

Here, a and a^+ are the annihilation and creation operators for the vibrational mode, $f(x)$ and $e(x)$ are functions of solvent coordinates. In the above equation, the first term is a constant, the second term is the off-diagonal linear coupling, and the third term is the diagonal quadratic coupling.

1. Harmonic oscillator

For a harmonic oscillator with $H_s=\omega_0(aa^+ +a^+a)/2$, we explicitly evaluate the temporal profile of vibrational relaxation and dephasing from second-order cumulant expansion of the solute-solvent interaction. The linear coupling to the solvent in Eq. (A1) yields the vibrational relaxation rate

$$\begin{aligned} k_n &= k(n\rightarrow n+1)+k(n\rightarrow n-1) \\ &= |\langle n|a^+|n+1|\rangle|^2 2\int_0^\infty e^{i\omega_{n,n+1}}\langle f(t)f(0)\rangle_b dt \\ &\quad + |\langle n|a^+|n-1|\rangle|^2 2\int_0^\infty e^{-i\omega_{n-1,n}}\langle f(0)f(t)\rangle_b dt, \end{aligned} \tag{A2}$$

where $\omega_{n+1,n}$ is the energy gap. The depletion rate out of the nth vibrational state can be separated into two parts: the rate for increasing one vibrational level $k(n\rightarrow n+1)$ and the rate for decreasing one vibrational level $k(n\rightarrow n-1)$. The two rate constants between a pair of adjacent levels satisfy the detailed balance relation.

For a linear harmonic oscillator, the frequency ω_0 is a constant independent of the quantum level, therefore $\omega_{n-1,n}=\omega_{n,n+1}=\omega_0$. We can write $k(n\rightarrow n+1)=(n+1)k_+$ and $k(n\rightarrow n-1)=nk_-$. Hence, the master equation for population relaxation is

$$\dot{P}_n=(n+1)k_-P_{n+1}+nk_+P_{n-1}-P_n[(n+1)k_++nk_-], \tag{A3}$$

which gives $\partial_t\overline{n}=-(k_--k_+)\overline{n}+k_+$ with $\overline{n}=\Sigma nP_n$ the average excitation number. Thus, we recover the equilibrium average $\overline{n}_{eq}=k_+/(k_--k_+)$ and the reactive rate $k=k_--k_+=\zeta(\omega_0)/\mu$, which is exactly the classical relaxation rate for the harmonic oscillator.

From the quadratic coupling, we can calculate the dephasing rate

$$\begin{aligned} k_{n,n+1} &= \tfrac{1}{2}\{|\langle n+2|a^+|n+1\rangle|^2-|\langle n|a^+|n-1\rangle|^2\} \\ &\quad \times\int_0^\infty \langle \delta e(t)\,\delta e(0)\rangle dt, \end{aligned} \tag{A4}$$

where $\delta e(t)=\partial^2V-\langle\partial^2V\rangle_b$ is the fluctuation in the curvature of the solute-solvent interaction. For a harmonic oscillator, the prefactor is a constant and the dephasing rate is constant.

Higher-order terms in the Taylor expansion of the solute-solvent interaction potential yields off-diagonal terms such as aa, a^+aa, etc., which are responsible for multiphoton processes. They become less important as the resonant frequency is multiples of the single photon frequency and gives much weak resonance with the low frequency bath. The linear terms can be incorporated in the first-order expression.

2. Anharmonic oscillator

For anharmonic oscillator, the energy gap decreases with the quantum number. The low frequency solvent has a stronger response at low frequency and the population relaxation rate increases with the quantum number. The dephasing rate is proportional to the zero frequency of the solvent spectrum and thus is dominated by the strength of the coupling matrix. At larger vibrational quantum numbers, the width of vibrational wave function broadens due to a stronger solute-solvent coupling. Thus, the pure-dephasing rate increases at larger vibrational quantum numbers.

For a harmonic oscillator, the linear coupling to the solvent results in vibrational relaxation, whereas the quadratic solute-solvent coupling results in vibrational dephasing. The situation is different for an anharmonic potential, for which the vibrational coordinate has both an off-diagonal part q_{OD}, giving rise to dissipation, and a diagonal part q_D, giving rise to pure dephasing. Formally, the solute coordinate operator can be expanded as

$$q=q_0+q_1(a+a^+)+q_2(aa^++a^+a)/2 + q_2'(aa+a^+a^+)/2+\cdots, \tag{A5}$$

where q_0, q_1, q_2, q_2' are expansion coefficients. Combined with Eq. (A1), the diagonal part of the solute-solvent interaction becomes

$$V_D=\frac{aa^++a^+a}{2}(-q_2\partial V+q_1\partial^2 V)+\cdots, \tag{A6}$$

which defines the quadratic fluctuating force $e=(-q_2\partial V+q_1\partial^2 V)$. It is well-known that the pure dephasing has two mechanisms: the quadratic coupling to the solvent and the anharmonicity in the solute vibrational mode. Below we demonstrate that these two mechanisms are essentially equivalent.

We now derive the anharmonicity-induced dephasing rate for the Morse potential $V(q)=D_e(1-e^{-\beta q})^2$, where D_e is the dissociation energy and β the inverse length scale. The fundamental frequency of the Morse oscillator is $\omega_0=\sqrt{2D_e\beta^2/\mu}$ and the total number of the bound states is $N/2$ with $N+1=\sqrt{8D_e\mu/\beta^2}=\chi_e^{-1}$. We use the following relation from Refs. 50 and 51:

$$b+b^+\approx\frac{N+1}{\sqrt{N}}\left[1-e^{-\beta q}-\frac{2}{\beta^2(N+1)^2}(e^{\beta q}p^2+p^2e^{\beta q})\right] \approx\chi_e^{-1/2}\beta q-\chi_e^{-1/2}\left[\frac{1}{2}\beta^2q^2+\frac{\beta^2p^2}{\mu^2\omega_0^2}\right], \tag{A7}$$

where $N+1\approx N$ for large N. The second-order contribution expressed with the creation and annihilation operators yields

$$b+b^+\approx q_1(a+a^+)+\beta q_1^2[\tfrac{1}{2}(a+a^+)^2-(a-a^+)^2], \tag{A8}$$

which has the diagonal components with $q_2=3\beta q_1^2$. Based on the definition in Eq. (A4), the pure-dephasing rate is

$$k'=q_2^2\int_0^\infty \mathrm{Re}\langle e(t)e(0)\rangle_b dt\approx\left(\frac{3\beta}{2\mu\omega_0}\right)^2 k_BT\hat{\eta}(0), \tag{A9}$$

where $\hat{\eta}(0)=\int_0^\infty\eta(t)dt$ is the integrated friction coefficient. The last expression is the classical limit of the dephasing rate first obtained by Oxtoby and later by many others.[62,63] To see this, we expand the Morse potential $V(q)=D_e\beta^2q^2-D_e\beta^3q^3+\cdots$ and identify the cubic coefficient $f_c=6D_e\beta^3$. Thus, the well-known result of $k'=f_c^2k_BT\hat{\eta}(0)/4\mu^4\omega_0^6$ is recovered.[63]

It should be noted that the dephasing rate differ by a factor of 9 if the momentum term in Eq. (A7) is neglected. Using the exact form for $a+a^+$ as the coupling to the solvent, it is possible to introduce linear dissipation without pure dephasing for an anharmonic oscillator. Such a coupling is not only a nonlinear function of coordinate but also a function of momentum. We thus conclude that for realistic systems the anharmonicity in vibrational modes contributes significantly to pure dephasing.

APPENDIX B: DISSIPATIVE HARMONIC OSCILLATOR COUPLED TO A QUANTUM BATH

In this appendix, we extend the previous discussion in Sec. III to a quantum bath. For simplicity, we assume the same dissipative harmonic oscillator as in Eq. (3.1). In this case, the quantum force-force correlation function is a complex function, $C_{qm}(t)=\langle f(t)f(0)\rangle=C_1(t)-iC_2(t)$, where the real part $C_1(t)$ is an even function and the imaginary part $C_2(t)$ is an odd function. The Fourier transform of the force-force correlation function is $\tilde{C}_{qm}(\omega)=\int_{-\infty}^{\infty}e^{i\omega t}C_{qm}(t)dt=\tilde{C}_1(\omega)-i\tilde{C}_2(\omega)$. The fluctuation-dissipation theorem requires

$$-i\tilde{C}_2(\omega)=\tanh\frac{\beta\hbar\omega}{2}\tilde{C}_1(\omega), \tag{B1}$$

where $\tilde{C}_2(\omega)$ is purely imaginary since $C_2(t)$ is an odd function. In the high temperature limit, $\tilde{C}_1(\omega)\to\tilde{C}_{cl}(\omega)$ and $\tilde{C}_2(\omega)\to0$.

Let us consider a quantum bath consisting of a number of harmonic oscillators $H_b=\Sigma_j(p_j^2/2m_j+m_j\omega_j^2x_j^2/2)$ and a bilinear system-bath coupling $H_{sb}=-q\Sigma_jg_jx_j$. For the harmonic bath, the quantum force-force correlation function is explicitly given as

$$C_{qm}(t)=\sum_j\frac{\hbar}{2m_j\omega_j}c_j^2\left[\coth\frac{\beta\hbar\omega_j}{2}\cos\omega_jt-i\sin\omega_jt\right], \tag{B2}$$

which reduces to the classical force-force correlation function $C_{\mathrm{cl}}(t)=\Sigma_jc_j^2/\beta m_j\omega_j^2\cos\omega_jt$ in the high temperature limit. Completing the Fourier transforms, one can readily show that[26,64]

$$\tilde{C}_1(\omega)=\frac{\beta\hbar\omega}{2}\coth\frac{\beta\hbar\omega}{2}\tilde{C}_{\rm cl}(\omega) \tag{B3a}$$

and

$$-i\tilde{C}_2(\omega)=\frac{\beta\hbar\omega}{2}\tilde{C}_{\rm cl}(\omega). \tag{B3b}$$

It is straightforward to prove that the transition moments given in Eq. (3.3) are still valid[39] given that $f(\tau)$ is now a complex variable. Following the same procedure as in Sec. III A, we derive the exact expression of the absorption profile as

$$A_{ge,\rm abs}(t)=e^{-i\omega_0 t}\times\frac{1+\alpha_{11}+\alpha_{22}}{[1+2(\alpha_{11}+\alpha_{22})+4(\alpha_{11}\alpha_{22}-\alpha_{12}\alpha_{12}^*)]^{3/2}}. \tag{B4}$$

This expression is almost identical to Eq. (3.4) except that α_{12} is a complex function. With the quantum force-force correlation function, we obtain the explicit expression of α_{12} as

$$\alpha_{12}=\frac{1}{2\mu\omega_0\hbar}\int_0^t d\tau\int_0^t d\tau'[C_1(\tau-\tau')\sin\,\omega_0(\tau+\tau')+iC_2(\tau-\tau')\sin\,\omega_0(\tau-\tau')]. \tag{B5}$$

Equation (B5) reduces to α_{12} in Eq. (3.4) in the classical limit when $C_2=0$.

In the perturbative approach, we follow the same procedure as in Sec. III B and obtain

$$\begin{aligned}A_{ge,\rm abs}(t)&\approx e^{-i\omega_0 t}\exp\left\{-\frac{1}{2}\int_0^t d\tau\int_0^t d\tau'[C_{qm}(\tau-\tau')\times\langle q(\tau)q(\tau')\rangle_e+C_{qm}^{\dagger}(\tau-\tau')\langle q(\tau)q(\tau')\rangle_g^{\dagger}]\right\}\\&\approx e^{-i\omega_0 t}\exp\left\{-\frac{1}{\mu\omega_0\hbar}\int_0^\tau d\tau\int_0^t d\tau'\times[2C_1(\tau-\tau')\cos\,\omega_0(\tau-\tau')-C_2(\tau-\tau')\times\sin\,\omega_0(\tau-\tau')]\right\}.\end{aligned} \tag{B6}$$

The first term in the exponent, which equals $2[\alpha_{11}(t)+\alpha_{22}(t)]$, is the classical perturbation result of Eq. (3.13) and the second term represents the quantum effects from the imaginary part of the force-force correlation function.

In the long-time limit, we invoke the Markovian approximation in the perturbative expression of Eq. (B6) and obtain $A_{n,n+1,\rm abs}(t)\approx e^{-i\omega_0 t}\exp[-(\Gamma_{n+1}+\Gamma_n)t/2]$, where $\Gamma_n=\int_0^\infty[2(n+1/2)C_1(\tau)\cos\,\omega_0\tau-C_2(\tau)\sin\,\omega_0\tau]d\tau$ is the population relaxation rate from the vibrational state n. Hence, the presence of the imaginary part of the quantum correlation function reduces the decay rate of the envelop, creating more coherent oscillations in absorption profile.

[1] A. Laubereau and W. Kaiser, Rev. Mod. Phys. **50**, 607 (1978).
[2] T. Elsaesser and W. Kaiser, Annu. Rev. Phys. Chem. **42**, 83 (1991).
[3] D. W. Oxtoby, Adv. Chem. Phys. **47**, 487 (1981).
[4] S. Mukamel, *Principles of Nonlinear Optical Spectroscopy* (Oxford University Press, New York, 1995).
[5] A. Tokmakoff, B. Sauter, and M. D. Fayer, J. Chem. Phys. **100**, 9035 (1994).
[6] J. C. Owrutsky, D. Raftery, and R. M. Hochstrasser, Annu. Rev. Phys. Chem. **45**, 519 (1994).
[7] G. R. Fleming and M. Cho, Annu. Rev. Phys. Chem. **47**, 109 (1996).
[8] W. P. de Boeij, M. S. Pshenichnikov, and D. A. Wiersma, Annu. Rev. Phys. Chem. **49**, 99 (1998).
[9] W. Zhao and J. C. Wright, Acta Radiol. **84**, 1411 (2000).
[10] T. S. Yang, M. S. Chang, R. Chang, M. Hayashi, S. H. Lin, P. Vohringer, W. Dietz, and N. F. Scherer, J. Chem. Phys. **110**, 12070 (1999).
[11] Z. Bihary, R. B. Gerber, and V. A. Apkarian, J. Chem. Phys. **115**, 2695 (2001).
[12] Y. Tanimura and S. Mukamel, J. Chem. Phys. **99**, 9496 (1993).
[13] B. J. Berne and R. Pecora, *Dynamic Light Scattering* (Wiley-Interscience, New York, 1976).
[14] Y. C. Sun, H. D. Gai, and G. A. Voth, J. Chem. Phys. **100**, 3247 (1994).
[15] B. M. Ladanyi and R. M. Stratt, J. Phys. Chem. A **102**, 1068 (1998).
[16] S. A. Egorov and J. L. Skinner, J. Chem. Phys. **105**, 7047 (1996).
[17] D. E. Sagnella, J. E. Straub, T. A. Jackson, M. Lim, and P. A. Anfinrud, Proc. Natl. Acad. Sci. U.S.A. **96**, 14324 (1999).
[18] K. F. Everitt, J. L. Skinner, and B. M. Ladanyi, J. Chem. Phys. **116**, 179 (2002).
[19] C. P. Lawrence and J. L. Skinner, J. Chem. Phys. **117**, 5827 (2002).
[20] R. Rey and J. T. Hynes, J. Chem. Phys. **104**, 2356 (1996).
[21] E. L. Sibert III and R. Rey, J. Chem. Phys. **116**, 237 (2002).
[22] R. Rey and J. T. Hynes, J. Phys. Chem. A **106**, 11993 (2002).
[23] Q. Shi and E. Geva, J. Phys. Chem. A **107**, 9059 (2003).
[24] S. A. Egorov, E. Rabani, and B. J. Berne, J. Phys. Chem. B **103**, 10978 (1999).
[25] M. Tuckerman and B. J. Berne, J. Chem. Phys. **98**, 7301 (1993).
[26] J. S. Bader, B. J. Berne, E. Pollak, and P. Hänggi, J. Chem. Phys. **104**, 1111 (1996).
[27] S. H. Lin, J. Chem. Phys. **61**, 3810 (1974).
[28] A. Nitzan, S. Mukamel, and J. Jortner, J. Chem. Phys. **60**, 3929 (1974).
[29] A. Nitzan and R. Silbey, J. Chem. Phys. **60**, 4070 (1974).
[30] R. F. Loring, Y. J. Yan, and S. Mukamel, J. Chem. Phys. **87**, 5840 (1987).
[31] Y. J. Yan and S. Mukamel, J. Chem. Phys. **94**, 179 (1991).
[32] S. Mukamel, Annu. Rev. Phys. Chem. **51**, 691 (2000).
[33] V. Chernyak and S. Mukamel, J. Chem. Phys. **114**, 10430 (2001).
[34] A. Tokmakoff, J. Phys. Chem. A **104**, 4247 (2000).
[35] J. Y. Sung and M. H. Cho, J. Chem. Phys. **113**, 7072 (2000).
[36] J. Y. Sung and R. J. Silbey, J. Chem. Phys. **115**, 9266 (2001).
[37] R. Karrlein and H. Grabert, J. Chem. Phys. **108**, 4972 (1998).
[38] T. Kato and Y. Tanimura, J. Chem. Phys. **117**, 6221 (2002).
[39] R. P. Feynman and A. R. Hibbs, *Quantum Mechanics and Path Integrals* (McGraw-Hill, New York, 1965).
[40] M. Kryvohuz and J. Cao (unpublished).
[41] R. Kosloff and S. A. Rice, J. Chem. Phys. **72**, 4591 (1980).
[42] S. Okazaki, Adv. Chem. Phys. **118**, 191 (2001).
[43] S. Hammes-Schiffer and J. C. Tully, J. Chem. Phys. **101**, 4657 (1994).
[44] S. A. Corcelli and J. C. Tully, J. Phys. Chem. A **106**, 10849 (2002).
[45] R. Kapral and G. Ciccotti, J. Chem. Phys. **110**, 8919 (1999).
[46] O. V. Prezhdo and P. J. Rossky, J. Chem. Phys. **107**, 825 (1997).
[47] D. F. Coker and L. Xiao, J. Chem. Phys. **102**, 496 (1995).
[48] N. Makri, J. Phys. Chem. B **103**, 2823 (1999).
[49] J. Cao, L. W. Ungar, and G. A. Voth, J. Chem. Phys. **104**, 4189 (1996).
[50] J. Wu and J. Cao, J. Chem. Phys. **115**, 5381 (2001).
[51] M. Kryvohuz and J. Cao, J. Chem. Phys. (submitted).
[52] J. Stenger, D. Madsen, P. Hamm, E. T. J. Nibbering, and T. Elsaesser, Phys. Rev. Lett. **87**, 027401 (2001).
[53] S. Woutersen, U. Emmerichs, H.-K. Nienhuys, and H. J. Bakker, Phys. Rev. Lett. **81**, 1106 (1998).
[54] A. Pakoulev, Z. H. Wang, Y. S. Pang, and D. D. Dlott, Chem. Phys. Lett. **380**, 404 (2003).
[55] C. J. Fecko, J. D. Eaves, J. J. Laparo, and A. Tokmakoff, Science **301**, 1698 (2003).
[56] J. B. Asbury, T. Steinel, C. Stromberg, S. A. Corcelli, C. P. Lawrence, J. L. Skinner, and M. D. Fayer, J. Phys. Chem. A **108**, 1107 (2004).

[57] S. Palese, S. Mukamel, R. J. D. Miller, and W. T. Lotshaw, J. Phys. Chem. **100**, 10380 (1996).
[58] M. Lim and R. M. Hochstrasser, J. Chem. Phys. **115**, 7629 (2001).
[59] M. Lim, P. Hamm, and R. M. Hochstrasser, Proc. Natl. Acad. Sci. U.S.A. **95**, 15315 (1998).
[60] G. Gnanakaran and R. M. Hochstrasser, J. Chem. Phys. **105**, 3486 (1996).
[61] E. L. Sibert III, W. P. Reinhardt, and J. T. Hynes, J. Chem. Phys. **77**, 3583 (1982).
[62] D. W. Oxtoby, Adv. Chem. Phys. **40**, 1 (1979).
[63] A. M. Levine, M. Shapiro, and E. Pollak, J. Chem. Phys. **88**, 1959 (1988).
[64] U. Weiss, *Quantum Dissipative Systems* (World Scientific, Singapore, 1999).